

# Molecular-Level Understanding of the Ro-vibrational Spectra of N<sub>2</sub>O in Gaseous, Supercritical and Liquid SF<sub>6</sub> and Xe

Kai Töpfer,<sup>†</sup> Debasish Koner,<sup>†,¶</sup> Shyamsunder Erramilli,<sup>‡</sup> Lawrence D. Ziegler,<sup>‡</sup>  
and Markus Meuwly<sup>\*,†,§</sup>

<sup>†</sup>*Department of Chemistry, University of Basel, Klingelbergstrasse 80, CH-4056 Basel,  
Switzerland*

<sup>‡</sup>*Department of Chemistry and the Photonics Center, Boston University, 8 St Mary's St,  
MA 02215, Boston*

<sup>¶</sup>*Department of Chemistry, Indian Institute of Technology Hyderabad, Sangareddy,  
Telangana 502285, India*

<sup>§</sup>*Department of Chemistry, Brown University, Providence, RI 02912, USA*

E-mail: m.meuwly@unibas.ch

# Abstract

The transition between the gas-, supercritical-, and liquid-phase behaviour is a fascinating topic which still lacks molecular-level understanding. Recent ultrafast two-dimensional infrared spectroscopy experiments suggested that the vibrational spectroscopy of  $\text{N}_2\text{O}$  embedded in xenon and  $\text{SF}_6$  as solvents provides an avenue to characterize the transitions between different phases as the concentration (or density) of the solvent increases. The present work demonstrates that classical molecular dynamics simulations together with accurate interaction potentials allows to (semi-)quantitatively describe the transition in rotational vibrational infrared spectra from the P-/R-branch lineshape for the stretch vibrations of  $\text{N}_2\text{O}$  at low solvent densities to the Q-branch-like lineshapes at high densities. The results are interpreted within the classical theory of rigid-body rotation in more/less constraining environments at high/low solvent densities or based on phenomenological models for the orientational relaxation of rotational motion. It is concluded that classical MD simulations provide a powerful approach to characterize and interpret the ultrafast motion of solutes in low to high density solvents at a molecular level.

# Introduction

Solvent-solute interactions and the coupled dynamics between solute molecules embedded in a solvent are central for understanding processes ranging from rotational and vibrational energy relaxation to chemical reactivity in solution.<sup>1,2</sup> Vibrational spectroscopy is a particularly suitable technique to follow the structural dynamics of "hot" solutes in their electronic ground state interacting with a solvent environment. Experimentally, 1d- and 2d-infrared spectroscopies provide measures of the strength and time scale of solvent-solute interactions that couple to the resonant rovibrational excitation.<sup>3</sup> These effects can also be probed directly by molecular dynamics (MD) simulations.<sup>4</sup> The comparison of computations and experiments is a sensitive test for the quality of the intermolecular interaction potentials and

provide a molecular-level understanding of energy transfer mechanisms. Furthermore, the entire structural dynamics at molecular-level detail is contained in the time dependent motion of all solution species involved from the MD trajectories and available for further analysis.

The understanding of solute equilibration in solvents including high density gases and supercritical fluids (SCFs) is also important from a more practical perspective. For example, controlling the outcome of combustion reactions which are often performed in the supercritical regime requires knowledge of energy transfer rates and mechanisms in high temperature and pressure solutions.<sup>5,6</sup> For reactions, it has been recognized that characterizing and eventually tuning the physico-chemical properties of the solvent can be as important as determining the best catalyst.<sup>6</sup> Hence, gaining molecular-level insight into the properties of solute-solvent dynamics is central not only for understanding fundamental solution interactions but also for industrial processes where solvents such as ionic, supercritical, or eutectic liquids are employed. On the other hand, the possibility to specifically manipulate dynamical properties in solvent system have been already successfully exploited in a wide range of applications.<sup>7,8</sup>

Linear and nonlinear optical and in particular infrared (IR) spectroscopy is a powerful means to characterize the structural and dynamical properties of condensed-phase systems. As an example, recent spectroscopic experiments in the Terahertz and infrared region combined with MD simulations provided an atomistically resolved picture of the structural properties of an eutectic mixture.<sup>9</sup> More broadly speaking, the structural and dynamical properties of solutions can and have been studied at a molecular level using two-dimensional IR (2DIR) spectroscopy through vibrational energy transfer.<sup>10-18</sup> The energy transfer rate for exchange of vibrational energy is expected to follow a 6th-power, distance dependent law,<sup>17</sup> similar to NOESY in NMR spectroscopy,<sup>19,20</sup> or Förster energy transfer between electronic chromophores.<sup>21</sup> As an example, the presence of cross-peaks in a 2D spectrum has been directly related to the formation of aggregated structures.<sup>11</sup> However, interpretation and

more in-depth understanding of the solvent structure requires additional information that can be obtained for example from MD simulations.

Recent 2DIR experiments on gas and supercritical phase solutions have shown how rotational energy returns to equilibrium following rovibrational excitation.<sup>22-24</sup> The dynamics of N<sub>2</sub>O as the spectroscopic probe surrounded by xenon atoms and SF<sub>6</sub> molecules has provided valuable information about density-dependent change in the solvent structure and energy transfer dynamics as the fluid approaches and passes through the near-critical point density region. The 1D and 2D spectra of the N<sub>2</sub>O asymmetric stretch ( $\nu_3$ ) in Xe and SF<sub>6</sub> exhibit a significant dependence on solvent density.<sup>23</sup> At low density, corresponding to SF<sub>6</sub> and Xe in the gas phase, the FTIR (1D) band shape of the asymmetric stretch vibration is that of gas-phase N<sub>2</sub>O with clearly resolved P- and R-band structure whereas at high solvent density of the liquid Xe or SF<sub>6</sub> solvent only a Q-branch-like absorption feature peaked at the pure vibrational transition frequency was observed. Because the solvent density  $\rho$  can be changed in a continuous fashion between gas and liquid densities, along a near-critical isotherm ( $T \sim 1.01T_c$ ) it is also possible to probe the intermediate, super-critical regime of the solvent. 2DIR spectral shapes as a function of waiting time and solvent density exhibit perfectly anti-correlated features that report on the  $J$ -scrambling or rotational energy relaxation rates.<sup>22-24</sup>

Given the molecular-level detail provided by quantitative MD simulations, the present work focuses on changes in the IR spectroscopy of N<sub>2</sub>O embedded in SF<sub>6</sub> and xenon and their interpretation at a structural level. For this, an accurate kernel-based representation of high-level electronic structure calculations for the spectroscopic reporter (N<sub>2</sub>O) is combined with state-of-the art treatment of electrostatic interactions employing the minimally distributed charge model (MDCM)<sup>25-27</sup> which captures multipolar interactions. Extensive MD simulations for densities corresponding to those used in the recent 1D and 2D experiments were carried out.

The current work is structured as follows. First, the Methods are presented. Next, the quality of the interaction potentials is discussed. Then, the density-dependent FTIR spectra are compared with experiments, the vibrational frequency fluctuation correlation functions are characterized and the organization of the solvent is analyzed for xenon and SF<sub>6</sub> as the solvents. Finally, the findings are discussed in a broader context.

## Methods

### Potential Energy Surfaces

The intramolecular potential energy surface (PES) of N<sub>2</sub>O in its electronic ground state (<sup>1</sup>A') is provided by a machine-learned representation using the reproducing kernel Hilbert space (RKHS) method.<sup>28,29</sup> Reference energies at the CCSD(T)-F12/aug-cc-pVQZ level of theory were determined on a grid of Jacobi coordinates ( $R, r, \theta$ ) with  $r$  the N-N separation,  $R$  the distance between the center of mass of the diatom and the oxygen atom, and  $\theta$  the angle between the two distance vectors. The grid in  $r$  contained 15 points between 1.6 a<sub>0</sub> and 3.1 a<sub>0</sub>, 15 points between 1.8 a<sub>0</sub> and 4.75 a<sub>0</sub> for  $R$ , and a 10-point Gauss-Legendre quadrature between 0° and 90° for  $\theta$ . All calculations were carried out using the MOLPRO package.<sup>30</sup>

The total energy is represented by a 3D kernel as

$$K(\mathbf{x}, \mathbf{x}') = k^{[2,6]}(R, R')k^{[2,6]}(r, r')k^{[2]}(z, z') \quad (1)$$

and the total PES is represented as  $V(\mathbf{x}) = \sum_{i=1}^N c_i K(\mathbf{x}, \mathbf{x}')$ . For more details the reader is referred to the literature.<sup>28</sup> Reciprocal power decay kernels

$$k^{2,6}(x, x') = \frac{1}{14} \frac{1}{x_{>}^7} - \frac{1}{18} \frac{x_{<}}{x_{>}^8} \quad (2)$$

were used for the radial dimensions ( $R$  and  $r$ ). Here,  $x_>$  and  $x_<$  are the larger and smaller values of  $x$  and  $x'$ , respectively. For large separations such kernels approach zero according to  $\propto \frac{1}{x^n}$  (here  $n = 6$ ) which gives the correct long-range behavior for neutral atom-diatom type interactions. For the angular coordinate a Taylor spline kernel  $k^{[2]}(z, z') = 1 + z_< z_> + 2z_<^2 z_> - \frac{2}{3} z_<^3$  is used where  $z = \frac{1 - \cos\theta}{2}$  and  $z_>$  and  $z_<$  are again the larger and smaller values of  $z$  and  $z'$ , defined similarly to  $x_>$  and  $x_>$ .

Intramolecular and intermolecular force field parameters for SF<sub>6</sub> are those from the work of Samios *et al.*<sup>31</sup> Intermolecular interactions are based on Lennard-Jones potentials only and the parameters are optimized such that MD simulations of pure SF<sub>6</sub> reproduce the experimentally observed  $PVT$  state points for liquid and gas SF<sub>6</sub>, as well as the states of liquid–vapor coexistence below and supercritical fluid above the critical temperature  $T_c$ , respectively. For xenon the parametrization for a Lennard-Jones potential from Aziz *et al.* was used that reproduces dilute gas macroscopic properties such as virial coefficient, viscosity and thermal conductivity over a wide temperature range but not specifically supercritical fluid properties.<sup>32</sup> As discussed further below, the critical concentration for xenon as determined from simulations (see Figure S1) was found to be 5.19 M compared with the experimentally reported value<sup>33,34</sup> of 8.45 M and variations for the critical temperature  $T_c$  for xenon compared with experiments can also be anticipated. In comparison, the critical concentration of  $\sim 5$  M for SF<sub>6</sub> from the present work (see below) matches the experimental value of 5.06 M<sup>33,34</sup> and is close to 5.12 M (obtained from the reported critical density of 0.74 g/ml) from the parametrization study.<sup>31</sup>

Electrostatic interactions are computed based on a minimally distributed charge model that correctly describes higher-order multipole moments of a molecule.<sup>25–27</sup> For parametrization, a reference electrostatic potential (ESP) of N<sub>2</sub>O in the linear equilibrium conformation is computed at the CCSD/aug-cc-pVTZ level using the Gaussian program package.<sup>35</sup> The

optimized MDCM fit reproduces the ESP with a RMSE of 0.31 kcal/mol. For SF<sub>6</sub> in its octahedral equilibrium conformation the ESP is computed at the MP2/aug-cc-pVTZ level of theory using the Gaussian program and the RMSE of the fitted ESP from MDCM is 0.11 kcal/mol. Recently,<sup>27</sup> non-iterative polarization was also included in MDCM, and this is also used here for N<sub>2</sub>O, SF<sub>6</sub> and Xe. The polarizability of linear N<sub>2</sub>O computed at the CCSD/aug-cc-pVTZ level is 2.85 Å<sup>3</sup> (with each atom contributing  $\sim 0.95$  Å<sup>3</sup> per atom), compared with 2.998 Å<sup>3</sup> from experiment.<sup>36</sup> For Xe at the CCSD/aug-cc-pVTZ the computed value of 2.96 Å<sup>3</sup> compares with 4.005 Å<sup>3</sup> from experiment.<sup>36</sup> For SF<sub>6</sub>, the experimentally measured polarizability of 4.49 Å<sup>3</sup> was used and evenly distributed over the fluorine atoms (0.74 Å<sup>3</sup> per F atom).<sup>37</sup>

The atomic van-der-Waals (vdW) parameters ( $\epsilon_i, R_{\min,i}$ ) of N<sub>2</sub>O were individually optimized to best describe the nonbonded interactions with SF<sub>6</sub> and Xe from comparing with energies from CCSD/aug-cc-pVTZ calculations for a number of N<sub>2</sub>O–SF<sub>6</sub> and N<sub>2</sub>O–Xe heterodimer structures. Lorenz-Berthelot combination rules of atomic vdW parameters between atom types  $i$  (solute) and  $j$  (solvent) ( $\epsilon_{ij} = \sqrt{\epsilon_i \epsilon_j}$  at an atom-atom distance of  $R_{\min,ij} = R_{\min,i}/2 + R_{\min,j}/2$ ) were used throughout. For the reference electronic structure calculations the grid was defined by center of mass distances between N<sub>2</sub>O and the solvent with range  $r = [2.0, 10.0]$  Å, and angles  $\alpha = [0, 180]^\circ$  with step size of 30° between the N<sub>2</sub>O bond axis and the N<sub>2</sub>O-solvent center of mass direction. Solute-solvent dimer structures with interaction energies lower than 5 kcal/mol above the dimer minimum structure were considered which led to 203 conformations for N<sub>2</sub>O–SF<sub>6</sub> whereas for N<sub>2</sub>O–Xe there were 102 structures. Then, the vdW parameters for each atom  $i$  of N<sub>2</sub>O were optimized to match the interaction energy predicted by CHARMM with the reference interaction energies from electronic structure calculations for the respective dimer conformations. The optimized vdW parameters are given in Table S2.

## Molecular Dynamics Simulations

Molecular dynamics simulations were performed with the CHARMM program package.<sup>38</sup> Each system (N<sub>2</sub>O in Xe and N<sub>2</sub>O in SF<sub>6</sub> at given temperature and solvent concentration) was initially heated and equilibrated for 100 ps each, followed by 10 ns production simulations in the *NVT* ensemble using a time step of 1 fs for the leapfrog integration scheme. The N<sub>2</sub>O/Xe systems were simulated at a temperature of 291.2 K and for N<sub>2</sub>O/SF<sub>6</sub> the temperature was 321.9 K which both are slightly above the experimental critical temperatures for condensation of xenon and SF<sub>6</sub>, respectively ( $T_c(\text{Xe}) = 289.74 \text{ K}$ ,  $T_c(\text{SF}_6) = 318.76 \text{ K}$ ).<sup>23,33,34</sup> A Langevin thermostat (coupling 0.1 ps<sup>-1</sup>) was used to maintain the temperature constant but was applied only to the solvent (Xe and SF<sub>6</sub>) atoms. Positions and velocities of snapshots of the simulations were stored every 1 fs for analysis. As intermolecular vibrational energy transfer is slow,<sup>24</sup> the structure of N<sub>2</sub>O was optimized and new velocities from a Boltzmann distribution at the simulation temperature were assigned to N<sub>2</sub>O after the heating step. This ensures that the kinetic energies along the asymmetric, symmetric and bending modes match the thermal energy with respect to the target simulation temperature.

The different simulation systems were prepared according to the conditions used in the experiments.<sup>22-24</sup> Table S1 summarizes the concentration  $c(\text{N}_2\text{O})$  of N<sub>2</sub>O, molar volumes  $V_m$  and critical density ratio  $\rho^* = \rho/\rho_c$ . The experimentally determined critical densities are  $\rho_c = 1.11 \text{ g/ml}$  for xenon and  $\rho_c = 0.74 \text{ g/ml}$  for SF<sub>6</sub> from which critical concentrations of 8.45 M and 5.06 M for xenon and SF<sub>6</sub> are obtained, respectively.<sup>33,34</sup> In all setups, the simulation box contains one N<sub>2</sub>O molecule and 600 Xe atoms or 343 SF<sub>6</sub> molecules which corresponds to similar simulation box volumes for similar relative density ratios of the two solvents. In the original parametrization study a simulation box containing 343 SF<sub>6</sub> molecules was used to fit temperature-pressure properties.<sup>31</sup>

In the MD simulations for N<sub>2</sub>O in SF<sub>6</sub>, electrostatic and polarization interactions were only

computed between the N<sub>2</sub>O solute and SF<sub>6</sub> solvent. Electrostatic and polarization contributions to the SF<sub>6</sub> solvent-solvent interactions were neglected. Such a procedure ensures that the pure (liquid, gas) properties of the solvent are unaltered. All force field parameters are listed in Table S2 in the supplementary information.

## Analysis

The line shape  $I(\omega)$  of the IR spectra for N<sub>2</sub>O in different solvent densities are obtained via the Fourier transform of the dipole-dipole correlation function from the dipole sequence of the single N<sub>2</sub>O molecule

$$I(\omega)n(\omega) \propto Q(\omega) \cdot \text{Im} \int_0^\infty dt e^{i\omega t} \sum_{i=x,y,z} \langle \boldsymbol{\mu}_i(t) \cdot \boldsymbol{\mu}_i(0) \rangle \quad (3)$$

A quantum correction factor  $Q(\omega) = \tanh(\beta\hbar\omega/2)$  was applied to the results of the Fourier transform.<sup>39</sup>

The response of the solute on the solvent structure and dynamics was evaluated by determining the frequencies of the quenched normal modes (QNM) of N<sub>2</sub>O for frames every 5 fs of the simulation. For QNM a short steepest descent geometry optimization for N<sub>2</sub>O within a frozen solvent conformation for either 100 steps or until the gradient root mean square of  $10^{-4}$  kcal/mol/Å was reached was carried out. The  $9 \times 9$  mass weighted Hessian matrix with regard to the solutes atom displacement in Cartesian coordinates was determined and diagonalized yielding time series of all 9 normal modes.<sup>40,41</sup> Instantaneous normal mode (INM) analyses were also applied on the solute by diagonalizing its mass weighted Hessian matrix without prior geometry optimization on N<sub>2</sub>O to obtain insights on the impact of the solvent structure on the translational and rotational modes of the N<sub>2</sub>O solute.<sup>40</sup>

The vibrational frequency-frequency correlation function (FFCF)  $\langle \nu_{\text{as}}(t) \cdot \nu_{\text{as}}(0) \rangle$  was computed for the time series of the asymmetric stretch frequency  $\nu_{\text{as}}$  gathered from the QNM analyses. The amplitude  $A$ , lifetimes  $\tau_i$  and offset  $\Delta$  of a bi-exponential function  $c(t) = Ae^{-t/\tau_1} + (1 - A)e^{-t/\tau_2} + \Delta$  were optimized to fit the normalized FFCF for  $t \in [0.1, 2.0]$  ps.

Radial distribution functions  $g(r)$  for solvent-solvent and solvent-solute pairs were determined from the average number of molecules  $\langle dn_r \rangle$  of type B within the shell in the range of  $r - \Delta r/2 < r \leq r + \Delta r/2$  around molecules of type A.

$$g(r) = \frac{1}{\langle \rho_{\text{local}} \rangle} \cdot \frac{\langle dn_r \rangle}{4\pi r^2 \Delta r} \quad (4)$$

Here,  $\langle \rho_{\text{local}} \rangle$  is the local density of compound B around compound A within a range that is half the simulation box edge length and the shell width was  $\Delta r = 0.1 \text{ \AA}$ . The average coordination number  $\langle N(r') \rangle$  of compounds B within range  $r'$  around compound A can be obtained from  $g(r)$  according to

$$\langle N(r') \rangle = 4\pi \langle \rho_{\text{local}} \rangle \int_0^{r'} g(r) r^2 dr \quad (5)$$

## Results

### Validation of the Interaction Potentials

First, the quality of the intramolecular PES for  $\text{N}_2\text{O}$  is discussed, followed by a description of the van der Waals parameters for the  $\text{N}_2\text{O}$  solute fit to the *ab initio* reference calculations.

The RKHS model provides a full-dimensional, intramolecular PES for  $\text{N}_2\text{O}$  which was orig-

inally developed for investigating the N+NO collision reaction dynamics.<sup>29</sup> The Pearson coefficient  $R^2$  of the RKHS representation and the full set of reference values is 0.99983 and the root mean squared error (RMSE) between RKHS and reference energies up to 20 kcal/mol above the equilibrium structure (78 reference energies) is 0.13 kcal/mol. To establish the spectroscopic quality of the PES, the evaluation by the discrete variable representation (DVR) method using the DVR3D<sup>42</sup> package yields a fundamental asymmetric stretch frequency of N<sub>2</sub>O of 2229 cm<sup>-1</sup> compared with 2224 cm<sup>-1</sup> from experiments in the gas phase.<sup>43-45</sup> The bending and symmetric stretch frequencies obtained from the DVR3D calculations are 598 cm<sup>-1</sup> and 1291 cm<sup>-1</sup>, respectively, and the overtone of the bending mode lies at 1184 cm<sup>-1</sup>. Experimentally, the bending and symmetric stretch are found at 589 cm<sup>-1</sup> and 1285 cm<sup>-1</sup>, respectively, while the overtone of the bending frequency is at 1168 cm<sup>-1</sup>.<sup>43-45</sup>

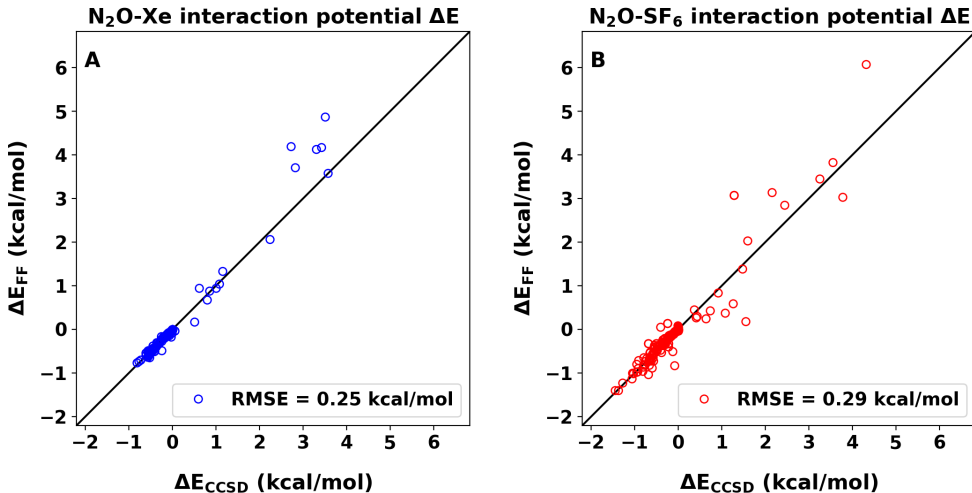


Figure 1: Correlation between the CCSD/aug-cc-pVTZ reference interaction energies for the (A) N<sub>2</sub>O–Xe pair for 102 different conformations and (B) N<sub>2</sub>O–SF<sub>6</sub> pair for 203 different conformations with interaction energies lower than 5 kcal/mol above the minimum, respectively.

Using MDCMs for the electrostatics of N<sub>2</sub>O in the two solvent environments (Xe and SF<sub>6</sub>) requires a readjustment of the solute vdW parameters. To keep the solvent-solvent interaction

unchanged, only the vdW parameters of N<sub>2</sub>O were optimized with respect to interaction energies from reference electronic structure calculations.

Figure 1 reports the correlation between reference and model interaction energies with optimized vdW parameters for N<sub>2</sub>O for the N<sub>2</sub>O–Xe (panel A) and N<sub>2</sub>O–SF<sub>6</sub> (panel B) complexes. The reference interaction energies  $\Delta E_{\text{CCSD}} = E_{\text{pair}} - E_{\text{solute}} - E_{\text{solvent}}$  are the differences between the respective total *ab initio* energy of the pair and the energies of the solute  $E_{\text{solute}}$  and solvent  $E_{\text{solvent}}$  fragment in a fixed minimum energy conformation. The force field energies  $\Delta E_{\text{FF}} = E_{\text{elec}} + E_{\text{LJ}}$  include electrostatic and polarization contributions, and the Lennard-Jones potential between the solute and solvent at the same conformation as in the reference data set. The energies sample attractive (negative energy) and repulsive (positive energy) ranges of the N<sub>2</sub>O–solvent energies and the comparison is restricted to energies within 5 kcal/mol of the separated molecules which is the zero of energy. For N<sub>2</sub>O–Xe, the RMSE is 0.25 kcal/mol and for N<sub>2</sub>O–SF<sub>6</sub> it is 0.29 kcal/mol. The most stable structure is stabilized by  $-1.41$  kcal/mol ( $-1.37$  kcal/mol from the fitted energy function) for N<sub>2</sub>O–SF<sub>6</sub>, and  $-0.80$  kcal/mol ( $-0.75$  kcal/mol) for N<sub>2</sub>O–Xe.

The critical concentration at which transition to a supercritical fluid occurs is another relevant property for the present work. Earlier work showed that this transition can be correlated with a pronounced increase in the local solvent reorganization lifetime  $\tau_{\rho}$ .<sup>46,47</sup> The quantity  $\tau_{\rho}$  is the integral over the local-density autocorrelation function  $\tau_{\rho} = \int_0^{\infty} C_{\rho}(t)dt$  and characterizes the time required for the local environment around a reference particle, e.g. the solute N<sub>2</sub>O in the present case, to change substantially. Hence,  $\tau_{\rho}$  can also be considered a local-density reorganization time.<sup>47</sup>

Figures S1 and S2 report the local solvent reorganization lifetimes  $\tau_{\rho}$  for pure xenon and SF<sub>6</sub>, respectively, from MD simulations. The solvent environments are defined by cutoff radii

which correspond approximately to the first and second minima of the solvent-solvent RDF, see Figure S4. For SF<sub>6</sub> the force field was parameterized<sup>31</sup> to reproduce the experimentally measured critical density with corresponding concentration  $c_{\text{crit}}(\text{SF}_6) = 5.06 \text{ M}$  at the critical temperature.<sup>33,34</sup> The present simulations yield a peak for  $\tau_\rho$  at  $c(\text{SF}_6) = 5.02 \text{ M}$ , in close agreement with the experimental critical concentration at the critical temperature and the concentration with the local peak in  $\tau_2$  in Figure 4D. For xenon, however, the parametrization of the PES<sup>32</sup> did not include phase transition properties to the supercritical regime. Figure S1 shows that the maximum in  $\tau_\rho$  occurs at  $c(\text{Xe}) = 5.19 \text{ M}$ . This compares with a critical concentration of 8.45 M at  $T_c$  from experiment.<sup>33,34</sup>

## Infrared Spectroscopy

The computed IR spectra for the N<sub>2</sub>O asymmetric ( $\nu_{\text{as}}$ ) stretch in xenon and SF<sub>6</sub> solution as a function of solvent density for near critical isotherms allows comparison between experimental and simulation results. The present work focuses mainly on the change of the IR line shape at different solvent concentrations especially the P-, Q-, and R-branch structure, see Figures 2 and 3. The P- and R-branches are the IR spectral features at lower and higher wavenumber from the pure vibrational transition frequency for the excitation of mode  $\nu$ . The  $\nu_{\text{as}}$ ,  $\nu_{\text{s}}$ , and  $\nu_{\delta}$  band shapes arise due to conservation of angular momentum during a vibrational excitation upon photon absorption.<sup>43</sup> The Q-branch is the absorption band feature at the transition frequency. In addition to the asymmetric stretch  $\nu_{\text{as}}$  ( $\sim 2220 \text{ cm}^{-1}$ , symmetry  $A_1/\Sigma^+$ ), the symmetric stretch  $\nu_{\text{s}}$  ( $\sim 1305 \text{ cm}^{-1}$ ,  $A_1/\Sigma^+$ ) and the bending vibration  $\nu_{\delta}$  ( $\sim 615 \text{ cm}^{-1}$ ,  $E_1/\Pi$ ) fundamentals from MD simulations are reported and analyzed as a function of solvent density.

From a quantum mechanical perspective, the rotational structure of an IR-active vibrational mode for a linear molecule (such as N<sub>2</sub>O) in the gas phase leads to P- and R-branches. Selection rules dictate the change of the rotational and vibrational quantum states,  $j$  and  $\nu$ ,

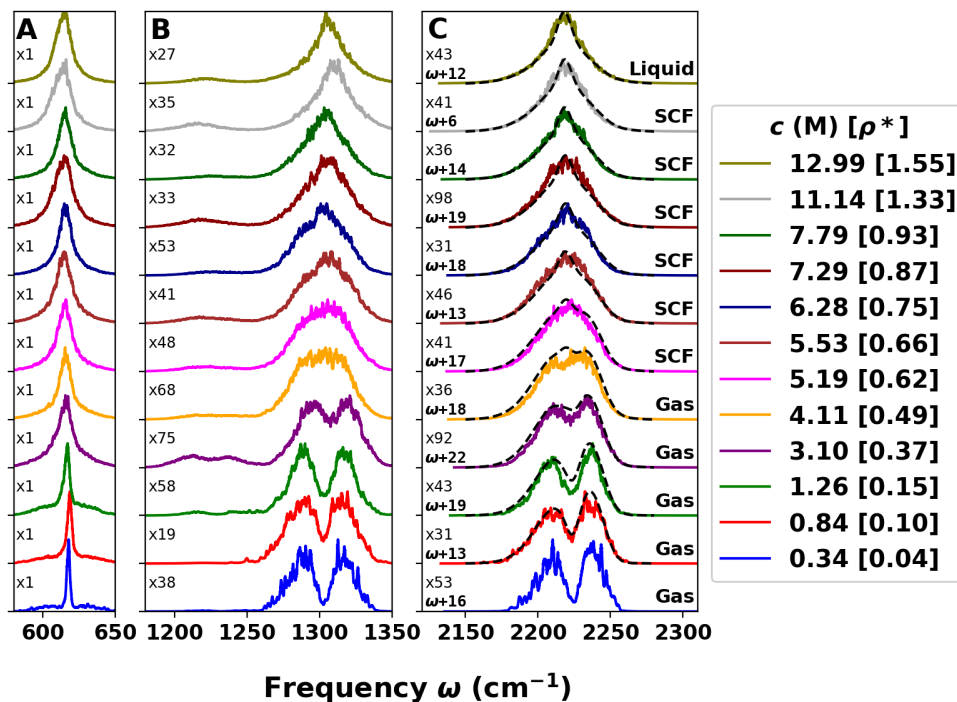


Figure 2: IR spectra of  $\text{N}_2\text{O}$  in xenon at different solvent concentrations for frequency ranges of (A)  $580\text{-}650\text{ cm}^{-1}$ , (B)  $1180\text{-}1350\text{ cm}^{-1}$  and (C)  $2120\text{-}2310\text{ cm}^{-1}$  at  $291.2\text{ K}$ . The amplitudes are scaled by the factor indicated at the center left for each range and density. In panel C the line shape frequency bands are shifted in frequency  $\omega$  to maximize the overlap with the experimental IR signal (dashed black lines, at  $291\text{ K}$  for gas, SCF, and at  $287\text{ K}$  for liquid xenon) at the corresponding density for the  $\text{N}_2\text{O}$  asymmetric stretch vibration. The frequency shift is also given in the bottom left corner, and an average shift is applied for densities without experimental reference spectra.

satisfying  $\Delta\nu = \pm 1$  and  $\Delta j = \pm 1$  for vibrational modes of  $A_1/\Sigma^+$  symmetry, and  $\Delta j = 0, \pm 1$  for vibrational modes of  $E_1/\Pi$  symmetry, respectively. For  $\text{N}_2\text{O}$ , the asymmetric  $\nu_{\text{as}}$  and symmetric stretch  $\nu_{\text{s}}$  are vibrational modes with parallel vibrational transition dipole moment to the bond axis and of  $A_1/\Sigma^+$  representation, and the bending mode  $\nu_{\text{b}}$  with perpendicular vibrational transition dipole moment of  $E_1/\Pi$  representation. These rotational selection rules are only strictly valid in the absence of perturbations (exact free rotor) and break down with increasing deviation from a free rotor model which, for example, can be due to embedding the rotor into a solvent of different density which is a means to tune the strength of the perturbation. As a consequence of the perturbation a Q-branch-like spectral feature emerges

for parallel bands and becomes dominant with a band maximum at the wavenumber of the corresponding pure vibrational transition energy at sufficiently high solvent density.

For N<sub>2</sub>O in xenon the IR band structure of  $\nu_{\text{as}}$  in Figure 2C ranges from resolved P- and R-branch in gaseous xenon up to a single near-Lorentzian-shaped band in liquid xenon in these classical MD simulations. From the simulations, at xenon concentrations higher than 5.19 M, or relative density of  $\rho^* = \rho/\rho_c = 0.62$ , the xenon solvent is a supercritical fluid. In the simulated absorption spectra at this density and above the  $\nu_{\text{as}}$  P- and R-band structure is not resolved and a centrally peaked band at the pure vibrational frequency dominates the band shape. The black dashed lines in Figure 2C are the experimentally determined spectra at the given solvent concentration.<sup>22-24</sup>

The agreement between experimental and computed N<sub>2</sub>O in Xe absorption band shapes is good and captures the dramatic gas phase-to-condensed phase lineshape change as a function of solvent density. However, the frequency position of the  $\nu_{\text{as}}$  band needs to be blue-shifted by a small frequency shift  $\omega$  to achieve the best overlap with the experimental IR line shape. The density dependent shifts are indicated in the panel and range from +6 to +22 cm<sup>-1</sup> with no discernible trend. The shift originates from different effects, including insufficient sampling of the amount and distribution of internal energy within the N<sub>2</sub>O solutes vibrational degrees of freedom, remaining small inaccuracies in the intermolecular interactions, neglecting many-body contributions, and slightly underestimating the anharmonicity in the PES along the relevant coordinates.

Figure 2B shows the corresponding band shape for  $\nu_{\text{s}}$  of N<sub>2</sub>O in Xe around 1305 cm<sup>-1</sup> in comparison to experimentally measured 1291 cm<sup>-1</sup> for N<sub>2</sub>O in the gas phase. Similar to  $\nu_{\text{as}}$ , it also displays resolved P- and R-branches at low solvent concentrations and changes into a Q-branch-like dominated structure in supercritical and liquid xenon. The IR band of the N<sub>2</sub>O

bending mode  $\nu_\delta$  appears at around  $615\text{ cm}^{-1}$  shown in Figure 2A, compared with  $589\text{ cm}^{-1}$  from experiment in the gas phase.<sup>43</sup> At low solvent concentrations the band structure of  $\nu_\delta$  from the MD simulations is a sharp Q-branch with weaker P- and R-branch side bands consistent with the quantum mechanical selection rules. The intensity of these bands are no longer evident relative to the central bending feature at higher solvent concentration. The first overtone of the  $\nu_\delta$  vibration is also detected between  $1220$  to  $1230\text{ cm}^{-1}$  in Figure 2B but with low intensity. The computed bending overtone ( $2\nu_b$ ) exhibits the same P- and R-branches at low density and the change to a single peaked band at high solvent concentration as observed for the  $\nu_s$  and  $\nu_{as}$  band structures, see Figures S5 and S6, in agreement with experimental results.<sup>48</sup>

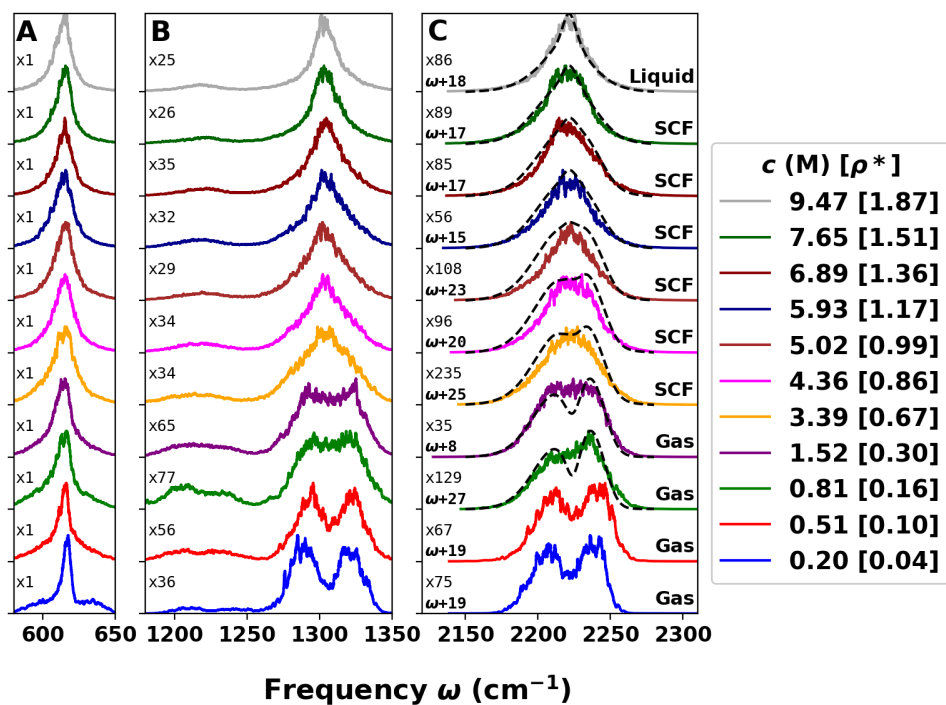


Figure 3: IR spectra of  $\text{N}_2\text{O}$  in  $\text{SF}_6$  at different solvent concentrations frequency ranges of (A)  $580\text{--}650\text{ cm}^{-1}$ , (B)  $1180\text{--}1350\text{ cm}^{-1}$  and (C)  $2120\text{--}2310\text{ cm}^{-1}$  at  $321.9\text{ K}$ . Further information are provided in the caption of Figure 2. The experimental IR signal (at  $322\text{ K}$  for gas, SCF, and at  $293\text{ K}$  for liquid  $\text{SF}_6$ ) at the corresponding density for the  $\text{N}_2\text{O}$  asymmetric stretch vibration are shown by the dashed black line.

The IR band structure of  $\nu_{\text{as}}$  of  $\text{N}_2\text{O}$  in  $\text{SF}_6$  is shown in Figure 3C. At the lowest solvent concentrations 0.20 M and 0.51 M ( $\rho^* = \{0.04, 0.10\}$ ) the simulated distinct P- and R-branch structure is evident but gradually disappears for  $[\text{SF}_6] > 1.52 \text{ M}$  ( $\rho^* > 0.30$ ) for corresponding experimental state points. As the solvent concentration of  $\text{SF}_6$  increases the band shape changes into a single peaked band in agreement with the experimental IR spectra for  $[\text{SF}_6] = 7.65 \text{ M}$  and  $9.47 \text{ M}$  ( $\rho^* = \{1.51, 1.87\}$ ). The computed IR spectra for  $0.81 \leq [\text{SF}_6] \leq 5.93 \text{ M}$  ( $0.16 \leq \rho^* \leq 1.17$ ) do not exhibit the double peak structure or are narrower compared to the experimental absorption spectra. The frequency position of the  $\nu_{\text{as}}$  band is also adjusted by a small frequency blue shift  $\omega$  within the range of  $+8$  to  $+27 \text{ cm}^{-1}$  to maximize the overlap with the experimental IR line shape.

The line shapes for the  $\nu_\delta$  and  $\nu_s$  vibrational modes are shown in Figures 3A and B as a function of  $\text{SF}_6$  concentrations. The  $\nu_s$  mode changes from P-/R-branches at low solvent concentrations into a single featured structure in supercritical and liquid  $\text{SF}_6$ . The calculated IR band of  $\nu_\delta$  around  $615 \text{ cm}^{-1}$  exhibits a sharp Q-branch with resolvable weak P- and R-branch satellites only at low  $\text{SF}_6$  concentration. The first overtone of the perpendicularly polarized  $\nu_\delta$  mode is again detected between  $1220$  to  $1230 \text{ cm}^{-1}$  with low intensity and a band shape as observed for the parallel polarized fundamental  $\nu_s$  and  $\nu_{\text{as}}$  band structures.

## Frequency-Frequency Correlation Function

The vibrational frequency fluctuation correlation function (FFCF) which probes the coupling of the solute vibrational modes to the solvent environment can be determined from 2DIR experiments. Of particular interest are the time scales of the lifetimes  $\tau_i$  and amplitudes  $A_i$  with which the FFCF decays which are shown in Figure S7. In the condensed phase, the FFCF is also related to the change of the center-line slope at different 2DIR waiting times.<sup>3</sup>

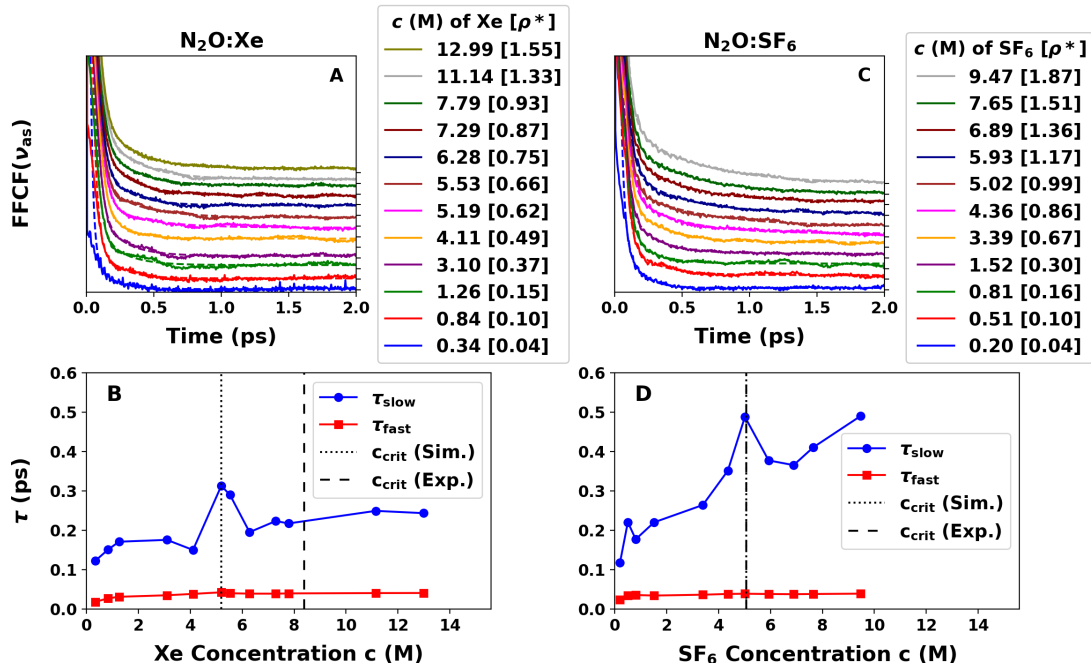


Figure 4: FFCF of the asymmetric stretch frequencies  $\nu_{\text{as}}$  of  $\text{N}_2\text{O}$  from QNM analysis in (A) xenon and (C)  $\text{SF}_6$  solvent at different concentrations. Asymptotically, all FFCFs decay close to zero ( $\Delta < 0.01$ ). An offset is added to the FFCF to avoid overlap and the lifetimes  $\tau$  from the fitted bi-exponential function are shown for the (B) xenon and (D)  $\text{SF}_6$  solvent depending on solvent concentration. The critical concentration  $c_{\text{crit}}$  determined from experiments and its estimation from simulations at  $T_c$  of xenon and  $\text{SF}_6$  are marked by the vertical dashed and dotted lines, respectively. It should be noted that the Xe–Xe interactions were not optimized to reproduce the experimentally known  $T_c$  for pure Xe whereas the model for  $\text{SF}_6$  does.

Figures 4A and C report the FFCFs for the asymmetric stretch  $\nu_{\text{as}}$  mode of  $\text{N}_2\text{O}$  in xenon and  $\text{SF}_6$  from QNM.<sup>1,49</sup> The fit of the FFCFs using a bi-exponential decay yields two times: a rapid inertial component ( $\tau_1 \sim 0.05$  ps) and a longer spectral diffusion time scale ( $\tau_2 \sim 0.2 \dots 0.5$  ps). These time scales compare with measured and computed time scales  $[\tau_1, \tau_2, \tau_3]$  for  $\text{CN}^-$  ([0.2, 2.9, n.a.] ps and [0.04, 0.87, 9.2] ps) and for  $\text{N}_3^-$  ([n.a., n.a.,  $\sim 1.2$ ] ps and [0.04, 0.23, 1.2] ps) in  $\text{H}_2\text{O}$ .<sup>49–52</sup> Here, "n.a." refers to time scales that were not determined or available from the experiments but clearly appeared in the analysis of the simulations. A similar behaviour of the vibrational FFCF as the one found in the present work - a first rapid relaxation time on the 0.05 to 0.1 ps time scale, followed by a slower time scale of 0.5 to 1.0 ps - was reported in an earlier MD simulation study for liquid  $\text{HCl}$ .<sup>53</sup>

It is important to note that experimentally decay times on the several 10 fs time scale are difficult to determine with confidence from vibrational FFCFs. Therefore only those longer than that are considered in the following. It is noted that for both ions ( $\text{CN}^-$  and  $\text{N}_3^-$ ) in water, mentioned above, the longer decay times are 1 ps or longer compared with  $\sim 0.5$  ps for  $\text{N}_2\text{O}$  in  $\text{SF}_6$ . This is consistent with the fact that ion–water interactions are considerably stronger than  $\text{N}_2\text{O}$ – $\text{SF}_6$  interactions. Furthermore, the  $\text{N}_2\text{O}$ –Xe interaction is weakest among all those considered here which leads to the rather short  $\tau_2$  value for this system, even relative to  $\text{SF}_6$ . Given that for the present system the intermolecular interactions are weak and the decay times are rapid it is anticipated that only  $\tau_2$  for  $\text{N}_2\text{O}$  in  $\text{SF}_6$  would be amenable to 2DIR experiments.

Figures 4B and D show the change of the low  $\tau_1$  and long lifetime  $\tau_2$  as a function of the xenon and  $\text{SF}_6$  solvent concentration, respectively. In both solvents, the longer lifetime slows with increasing concentration and a peak in the lifetime at 5.19 M in Xe and 5.02 M in  $\text{SF}_6$  is observed. The pronounced increase in  $\tau_2$  is likely to be related to approaching the critical point as the local peak in  $\tau_2$  at a  $\text{SF}_6$  solvent concentration of 5.02 M matches the critical concentration for pure  $\text{SF}_6$ . However, The local peak for  $\tau_2(c)$  for  $\text{N}_2\text{O}$  in Xe at 5.19 M is consistent with a critical concentration at 5.19 M for pure SCF xenon which is, however, far below the experimental critical concentration of 8.45 M. It is also noted that the slope for  $\tau_2(c)$  for  $\text{N}_2\text{O}$  in  $\text{SF}_6$  is considerably steeper than for Xe as the solvent. This is most likely also due to the increased solvent-solute interaction strength between  $\text{N}_2\text{O}$  and  $\text{SF}_6$  compared with Xe. The results for  $\tau_2$  indicate that interesting dynamical effects, such as critical slowing, can be expected to develop around the critical point of the solvent. It is worthwhile to note that at the critical concentration  $c(\text{Xe}) = 5.19$  M for the transition to a SCF the spectroscopy of the asymmetric stretch changes from P-/R-branches to Q-branch-like (Figure 2) and the decay time  $\tau_2$  from the FFCF of the asymmetric stretch (see Figure 4B) features a pronounced maximum. The fact that for xenon the critical density from the simulations is underestimated

(5.19 M vs. 8.45 M from experiments) but the concentration-dependence of the spectroscopy agrees with experiment suggests that orientational relaxation and inhomogeneous effects play the dominant role for the density dependence of the dipole correlation function.

## Radial Distribution Functions and Size of the Solvent Shells

A structural characterization of the solvent environment is afforded by considering the radial distribution functions  $g(r)$  between the center of mass of  $\text{N}_2\text{O}$  and the central sulfur atom and the Xe atom, which are shown in Figure S3A and C, respectively. They reveal a pronounced first solvation shell around the  $\text{N}_2\text{O}$  solute within  $\sim 4.3 \text{ \AA}$  (panel A) for the xenon and  $\sim 4.6 \text{ \AA}$  (panel C) for the  $\text{SF}_6$  solvent.

A more concise comparison of how the solvent environment depends on solvent density can be obtained by considering the average coordination number  $\langle N(r') \rangle$  of the Xe and  $\text{SF}_6$  solvent within the first solvation shell (Figures 5A and B) that are computed from the respective  $g(r)$ , see Figure S3. At the respective lowest sampled solvent concentration,  $\langle N(r') \rangle$  yields an average of 0.31 Xe atoms (panel A at 0.34 M) and 0.29  $\text{SF}_6$  molecules (panel B at 0.20 M) within the first solvation shell. The coordination number rises monotonically with increasing solvent concentration but shows a decrease in the slope within the SCF regime as the solvation shell fills. It is interesting to note that both solvents exhibit two slopes for  $N(r)$  depending on  $c$ : a first, steeper one for the gas-phase-like solvent into the SCF regime, and a second, flatter one, leading into the liquid-like regime. The slopes for the gas-phase-like regime is steeper ( $1.40 \text{ M}^{-1}$ ) for  $\text{SF}_6$  than for Xe ( $0.94 \text{ M}^{-1}$ ), which may be related to the solvent-solute interaction strength. The independent binary collision model (IBC)<sup>54,55</sup> predicts that the size of the solvent shell depends in a linear fashion on density over the entire concentration range where it is valid. For the lower densities this is indeed what is found but towards higher densities another, linear dependence develops with lower slope for both solvents. The

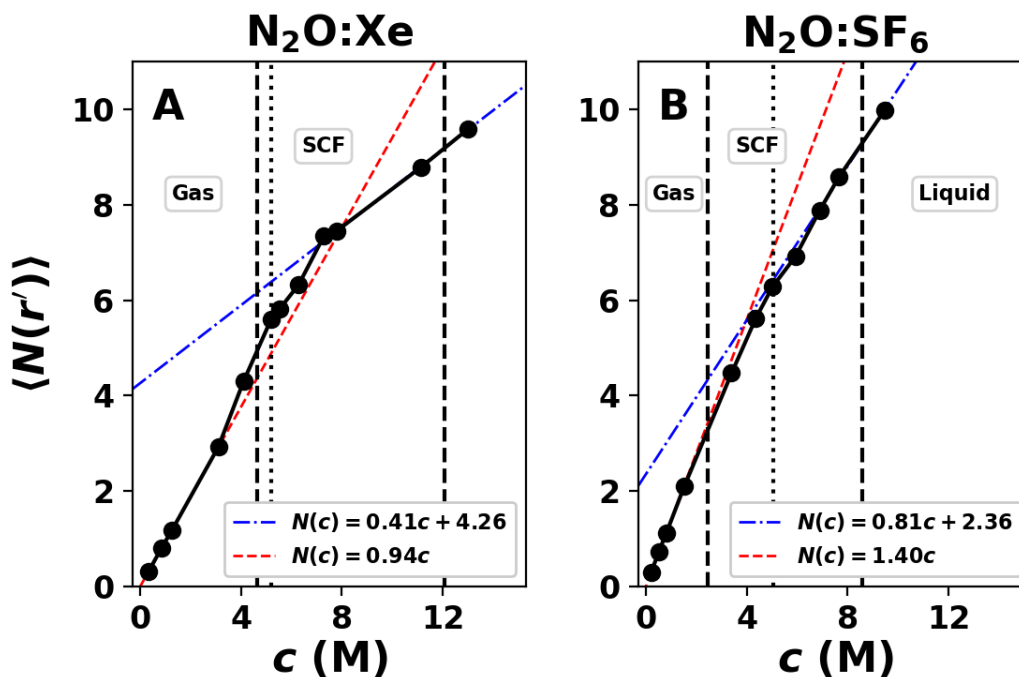


Figure 5: Average coordination number  $\langle N(r') \rangle$  of (A) the Xe ( $r' = 6.5 \text{ \AA}$ ) and (B) SF<sub>6</sub> solvent compounds ( $r' = 7.5 \text{ \AA}$ ) within the first solvation shell around N<sub>2</sub>O at cutoff distance  $r'$ . The red and blue lines are a linear fit of the first and last 3 data points, respectively. The vertical dotted lines mark the estimation of the critical concentration in the simulations at  $T_c$  of (A) xenon and (B) SF<sub>6</sub>, respectively, and the vertical dashed lines mark the approximate concentrations of the solvent phase transition.

breakdown of the IBC model occurs at higher solvent concentration for Xe than for SF<sub>6</sub> ( $c(\text{Xe}) \sim 8 \text{ M}$  vs.  $c(\text{SF}_6) \sim 5 \text{ M}$ , see Figure 5) compared with values of 4.1 M and 3.4 M from experiments, respectively.<sup>24</sup>

## Discussion

Classical MD simulations have been previously used to determine and analyze rotational vibrational spectra of simple solutes, including CO or HCl in a solvent (Argon)<sup>56,57</sup> or for water.<sup>58</sup> These calculations demonstrated that classical MD simulations are capable of

realistically capturing P- and R-branch structures in moderate to high density gases and even in liquid water.<sup>58</sup> Along similar lines, the present MD simulations of N<sub>2</sub>O in xenon or SF<sub>6</sub> as the solvent reproduce well the experimentally observed splitting in P-, Q- and R-branches and the overall lineshapes in the IR spectra of N<sub>2</sub>O depending on solvent concentration (see Figures 2 and 3). The agreement in the computed line shapes of the FTIR  $\nu_{\text{as}}$  spectrum of N<sub>2</sub>O in xenon does match with the experimental spectra as a function of solvent concentration. The separation between the maxima of the P- and R-branches is  $\sim [27, 25, 29, 22] \text{ cm}^{-1}$  at  $[0.34, 0.84, 1.26, 3.10] \text{ M}$  from the simulations, compared with  $\sim [25, 25, 22] \text{ cm}^{-1}$  at  $[0.84, 1.26, 3.10] \text{ M}$  from the experiments. The IR signals for the  $\nu_{\text{as}}$  vibration of N<sub>2</sub>O in SF<sub>6</sub> show a larger contribution of the Q-branch-like feature at lower  $\rho^*$  compared to that observed in the experimental spectra. For simulations in both solvents the computed spectra are shifted to the red compared with the results from experiments for  $\nu_{\text{as}}$ .

The computed IR spectra from the classical MD simulations of N<sub>2</sub>O/Xe in Figure 2 agree with the relative intensity and band width of the  $\nu_{\text{as}}$  vibration signal at the corresponding solvent concentration. The IR spectra of N<sub>2</sub>O in SF<sub>6</sub> in Figure 3 deviate more from the corresponding experimental line shapes by overestimating solvent-solute interactions, leading to a somewhat stronger contribution of the Q-branch-like absorption character at lower solvent concentration. The experimental  $\nu_{\text{as}}$  signal at the lowest measured solvent density of 0.81 M overlaps better with the computed signal at lower solvent densities of 0.51 M and 0.20 M. However, the line shape in highly dense supercritical and liquid SF<sub>6</sub> agrees well with experiment where the Q-band-like feature dominates the spectral lineshape and resolvable P- and R-branch contributions are not evident. At the same absolute density the asymmetric stretch of N<sub>2</sub>O is indicative of a more liquid-like character of SF<sub>6</sub> as the solvent compared with xenon, see Figures 2C and 3C.

Splitting of the IR spectrum into P- and R-branches correlates with free rotor properties of

the N<sub>2</sub>O solute molecule. Based on this, the results in Figure 3 indicate an overestimation of the solute-solvent interaction in SF<sub>6</sub> because a merged line shape for  $\nu_{\text{as}}$  arises between 0.81 M and 1.52 M from the computations whereas experimentally, this occurs for concentrations between 3.39 M and 4.36 M. Consequently, the rotation of N<sub>2</sub>O in the simulations starts to become hindered at lower solvent densities compared to experiment. This observation correlates with the long-range and stronger electrostatic interaction between N<sub>2</sub>O and polar SF<sub>6</sub> rather than xenon as the solvent.

As a comparison, the electrostatic contribution to the interaction energy of a N<sub>2</sub>O/SF<sub>6</sub> pair in its equilibrium conformation with  $-1.42$  kcal/mol is considerably stronger than the polarization contribution in an N<sub>2</sub>O/Xe pair with  $-0.84$  kcal/mol. As the electrostatic MDCM and vdW parameter fit are only applied to single molecules or molecule pairs, respectively, the energy function might insufficiently capture many-body interactions between the N<sub>2</sub>O solute and multiple SF<sub>6</sub> solvent molecules.

An overtone of the  $\nu_{\delta}$  vibration ( $615\text{ cm}^{-1}$ ) of N<sub>2</sub>O is found at about twice the frequency between  $1220$  to  $1230\text{ cm}^{-1}$  in both solvents. The splitting into P- and R-branches at low solvent densities originates from excitation of simultaneously two bending mode quanta ( $2\nu_{\delta}$ ) and the change of the rotational state by  $\Delta J = \pm 1$ .<sup>59,60</sup> Consequently, as the splitting of the  $2\nu_{\delta}$  IR band depends on the free rotor properties such as for the  $\nu_{\text{as}}$  and  $\nu_{\text{s}}$  IR band structure, the band shape changes towards a single Q-branch peak at higher solvent concentrations. In other words, the rotational “selection rules” followed by the bending overtone are the same as for the asymmetric stretch vibration which both have the same symmetry. This quantum mechanical result is seen in the present classical MD simulations.

The perturbation of the rotational modes by the solvent are visualized by the INM in Figures S8A and B for N<sub>2</sub>O in SF<sub>6</sub> and xenon at different densities, respectively. The INM histogram

for N<sub>2</sub>O in SF<sub>6</sub> shows two peaks around the zero frequency line for low positive and imaginary frequencies (positive and negative second derivative of the potential projected along normal mode displacement, respectively). The increasing shoulder of the INM histogram indicates higher barriers for the frustrated translational but also rotational normal modes as solvent density increases and, thus, larger deviations from a free rotor. The INM histogram for N<sub>2</sub>O in xenon in Figure S8B shows less narrow peaks and lower shoulder for gaseous solvent in comparison with the INM distribution of N<sub>2</sub>O in SF<sub>6</sub> in Figure S8A. The higher mode density around low frequencies for the INMs of N<sub>2</sub>O in xenon relative to SF<sub>6</sub> also indicates lower perturbation of free rotor character in gaseous and supercritical xenon solvent than SF<sub>6</sub>.

The change of the IR spectra for linear molecules in gaseous, supercritical up to liquid solvents can be compared with the experimental and theoretical work on hydrogen cyanide in an electric field.<sup>61,62</sup> With increasing field strength, the molecules evolve from a free rotor to those trapped in pendular states which is one way to control the population of rotational states in molecular beam experiments. The electric field lifts the degeneracy of the quantum number  $m_j$  (the projection of the angular momentum on the electric field direction) for each rotational state  $j$  and leads to a manifold of different transitions that corresponds to the IR spectra. Pendular states are linear combinations of field-free  $(j, m_j)$  states covering a range of  $j$ -values but sharing the same  $m_j$  quantum number, i.e.  $j$ -mixing occurs.<sup>61</sup> With increasing electric field strength the field-free selection rule  $\Delta j = \pm 1$  breaks down. For excitation along dipole transition vectors parallel to the electric field the P- and R-branch change into a single Lorentzian-shaped Q-branch at large electric field strength.<sup>61</sup>

The effects found for polar molecules in external electrical fields can be compared with the motion of N<sub>2</sub>O in a supercritical or liquid solvent. Here, the solvent molecules form a cavity around the solute where the direction of the angular momentum is not energetically degenerate and N<sub>2</sub>O behaves like in a pendular state. In analogy to a molecule in an electric field, the

P- and R-branches collapse into a single Q-branch-like band structure for vibrational modes with transition dipole moments perpendicular to the angular momentum of the molecule upon breakdown of the usual selection rules.

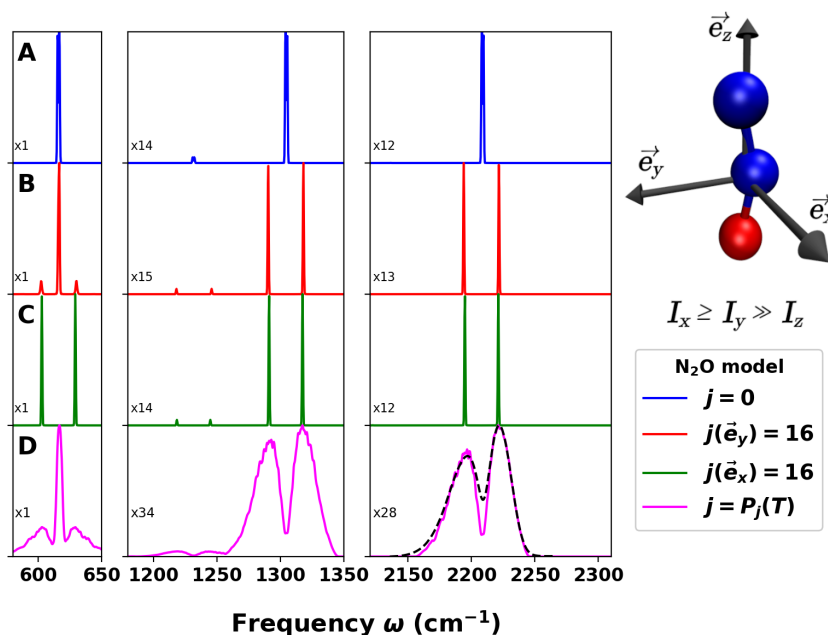


Figure 6: Model IR spectra from 100 ps MD simulations of a single  $\text{N}_2\text{O}$  molecule with vibrational energy equivalent to  $T = 321.9\text{ K}$  and either (A) no rotational energy, rotation around axis (B) perpendicular ( $\vec{e}_x$ ) or (C) parallel ( $\vec{e}_y$ ) to the transition dipole moment of the bending vibration of  $\text{N}_2\text{O}$ . Panel D shows a superposition of  $\text{N}_2\text{O}$  IR spectra from MD simulation at different rotational states  $j$  scaled by the respective probability according to the Maxwell-Boltzmann distribution  $P_j$  at  $T = 321.9\text{ K}$ . The experimental spectra of  $\text{N}_2\text{O}$  in gaseous  $\text{SF}_6$  ( $c = 1.26\text{ M}$ ) is shown by the dashed line and shifted by  $-14.5\text{ cm}^{-1}$  to maximize the overlap with the computed line shape. An illustration of an angles  $\text{N}_2\text{O}$  molecule with the principle axis of inertia are shown in the top right corner and the order of the moments of inertia  $I$ .

The IR spectra derived from classical MD simulations can also be analyzed following a model by Skinner *et al.* who considered the dipole-dipole correlation function  $\phi = \phi_{\text{vib}} \cdot \phi_{\text{rot}}$  as a product ansatz of a vibrational  $\phi_{\text{vib}}$  and a rotational component  $\phi_{\text{rot}}$ .<sup>58</sup> The composition of the IR band by P/R-branch and Q-branch depends on the angle  $\theta$  between the vibrational transition vector and the rotational axis. Assigning the vibration and rotation with an angular

frequency  $\omega_{\text{vib}}$  and  $\omega_{\text{rot}}$ , the time-dependence of the correlation function  $\phi(t)$  for an idealized classical rotor (without damping) has been expressed as

$$\phi(t) = \cos \theta \cdot \exp(i\omega_{\text{vib}}t) + (1 - \cos \theta) \cdot \exp(i(\omega_{\text{vib}} \pm \omega_{\text{rot}})t) \quad (6)$$

which assumes constant angular velocity, an approximation that does not necessarily hold for vibrating molecules.<sup>58</sup> The Fourier transform of  $\phi(t)$  in equation 6 leads to one Q-branch signal at  $\omega_{\text{vib}}$  for parallel alignment of the rotational axis and vibrational transition dipole vector ( $\cos \theta = 1$ ) and two P- and R-branch signals at  $\omega_{\text{vib}} - \omega_{\text{rot}}$  and  $\omega_{\text{vib}} + \omega_{\text{rot}}$  for perpendicularly aligned rotational axis and vibrational transition dipole vector ( $\cos \theta = 0$ ). For other cases or an unstable rotation axis, signals for all P-, Q- and R-branches arise in the IR spectra.

Figure 6 shows computed IR spectra from the Fourier transform of the dipole-dipole correlation function from MD simulations of a single N<sub>2</sub>O molecule with different initial conditions. For all cases (A-D) intramolecular energy is distributed along all vibrational normal modes with respect to the thermal energy at 321.9 K. Without any rotational energy assigned the IR spectra in Figure 6A shows no split into P- and R-branches. With rotational energy assigned around rotational axis *parallel* to the transition dipole vector the IR spectra in Figure 6B shows separation into P- and R-branches by 28 cm<sup>-1</sup> for  $\nu_{\text{as}}$  stretch that correlates for a rotational constant of  $B_{j=16} = 0.43$  cm<sup>-1</sup>. The IR signal of the bending mode primarily consists of the Q-branch with two small P- and R-branch satellites separated by  $\pm 14$  cm<sup>-1</sup> each from the Q-branch. For rotational energy assigned around a rotational axis *perpendicular* to both stretch and bending transition dipole moments all IR signals in Figure 6C split in P- and R-branches as well ( $B_{j=16} = 0.42$  cm<sup>-1</sup>) but no Q-branch is observed. The rotational energy corresponding to the rotational quantum state  $j = 16$  is the state with the highest probability according to the Maxwell-Boltzmann distribution function  $P_j(T)$  for N<sub>2</sub>O at 321.9 K.

At lower solvent density, the appearance of P-, Q- and R-branch in the model IR spectra in Figure 6B can be explained by the mechanical instability of a rotation around the transition dipole vector of the bending mode  $e_y$ . For bent  $\text{N}_2\text{O}$  the moments of inertia are ordered by  $I_x > I_y \gg I_z$ . According to the tennis racket theorem<sup>63</sup> the rotation around the axis  $e_y$  with the middle moment of inertia is unstable. Thus, the angle between rotation axis or angular momentum vector and the transition dipole vector of the bending mode varies in time and gives rise to P-, Q- and R-branch signals.

A superposition of model IR spectra at varying rotational energy states and randomly sampled rotation axis but perpendicular to the  $\text{N}_2\text{O}$  bond axis yields a line shape close to the computed spectra of  $\text{N}_2\text{O}$  in gaseous solvent at lower concentrations. The contribution of the single IR spectra at rotational state  $j$  to the model spectra in Figure 6D are scaled by the probability value according to  $P_j(T = 321.9 \text{ K})$ . An average rotational constant  $B = 0.42 \text{ cm}^{-1}$  is computed from the spectra with rotational states  $j = [2, 26]$ , which is in perfect agreement of the experimentally determined rotational constant of  $B_{\text{exp}} = 0.419 \text{ cm}^{-1}$ .<sup>64</sup> Hence, overall two regimes can be distinguished: for low densities the rotational motion of the solute is oscillatory and guided by the mechanical instability around the middle rotational axis (tennis-racket theorem) whereas at higher densities the constraining effect of the solvent due to tighter packing leads to a more diffusive rotational motion of the solute.

For additional clarification for how the transition between P-/R-features and Q-branch-like lineshapes occurs two different models are briefly considered. The first one operates directly on the dipole-dipole correlation function of a single  $\text{N}_2\text{O}$  molecule whereas the second one uses a Langevin-type simulation of one  $\text{N}_2\text{O}$  molecule in the gas phase. The influence of a solvent can be heuristically included by multiplication of the dipole-dipole correlation function  $\phi(t)$ , see Eq. 6, with an exponential damping, i.e. considering  $\phi(t) \times \exp(-t/\tau)$ .

The damping with characteristic time  $\tau$  models all sources of the dipole correlation function decay, primarily the solvent density dependence on orientational relaxation due to collisions between  $\text{N}_2\text{O}$  and the solvent in the present case. With increasing density of the solvent, for example,  $\tau$  decreases, which leads to loss of knowledge about its rotational motion as well as broadening of the computed IR signals, see Figure 7A. Consequently, the P-/R-features collapse into a single Q-branch-like peak for relaxation decays  $0.1 \leq \tau \leq 0.2$  ps which are considerably shorter than the rotational periods.

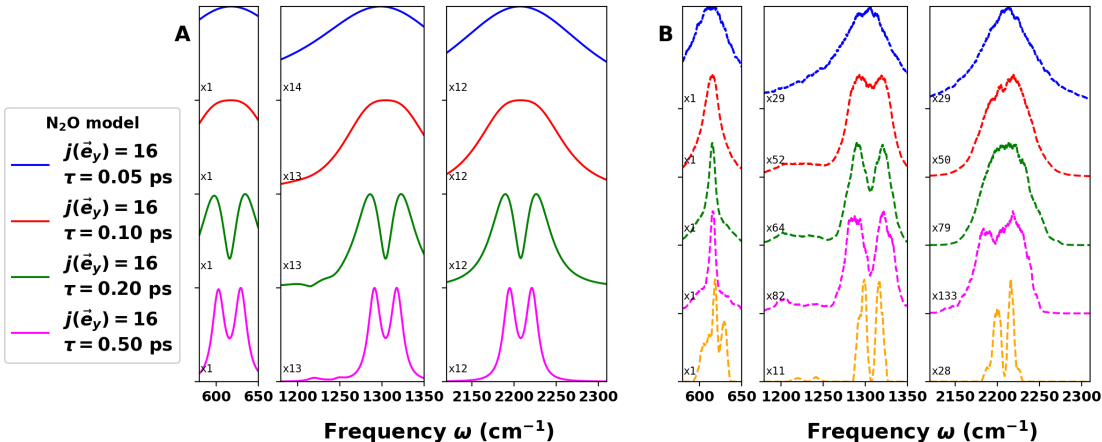


Figure 7: Panels A: Model IR spectra from a Fourier transform of the dipole-dipole correlation function multiplied by an exponential damping factor with  $\tau$  which describes orientational (rotational) relaxation and inhomogeneous effects. The dipole-dipole correlation function is obtained from a 100 ps MD simulation of a single  $\text{N}_2\text{O}$  molecule with vibrational energy equivalent to  $T = 321.9$  K and rotation around the axis parallel ( $\vec{e}_y$ ) to the transition dipole moment of the bending vibration of  $\text{N}_2\text{O}$ . Panel B: Model IR spectra from 10 ns Langevin simulations of a single  $\text{N}_2\text{O}$  molecule with initial vibrational and rotational energy equivalent to  $T = 321.9$  K. A Langevin thermostat with different friction coefficients  $\gamma_i = \{10, 1, 0.1, 0.01, 10^{-4}\}$   $\text{ps}^{-1}$  (from top to bottom) was applied to the dynamics to model energy exchange between  $\text{N}_2\text{O}$  and the solvent.

Alternatively, interaction with a solvent can be modelled from MD simulations with a stochastic thermostat, such as in Langevin dynamics, which applies random forces on the atoms to simulate orientational interactions with the heat bath. For this, 10 ns Langevin simulations with varying coupling strengths  $\gamma$  were run for a single  $\text{N}_2\text{O}$  molecule in the gas phase using

CHARMM and the dipole-dipole correlation function was determined. Figure 7B shows the computed IR spectra. At low coupling strength  $\gamma_i = 10^{-4} \text{ ps}^{-1}$  the IR spectra still yield a split of the asymmetric stretch into P- and R-branches (yellow trace). With increasing friction  $\gamma_i = 0.01 \text{ ps}^{-1}$  still multiple peaks are visible in the asymmetric stretch absorption lineshape but the spectral Q-branch-like region is getting filled in (pink trace). At yet higher  $\gamma_i \geq 0.1 \text{ ps}^{-1}$  (green, red, blue traces) the P-/R-features wash out entirely.

Finally, it is of some interest to discuss the results on the spectroscopy (Figures 2 and 3) and the solvent structure (Figure 5) from a broader perspective. The interaction between  $\text{N}_2\text{O}$  and Xe is weaker by about 50 % than that between  $\text{N}_2\text{O}$  and  $\text{SF}_6$ . The type of interaction also differs: pure van der Waals (in the present treatment) for Xe versus van der Waals and electrostatics for  $\text{SF}_6$ . It is interesting to note that the transition between the P-/R- and the Q-band-like spectra in Xe occurs at  $\rho^* \sim 0.6$  ( $\sim 5.2 \text{ M}$ ) compared with  $\rho^* \sim 0.2$  ( $\sim 0.9 \text{ M}$ ) for  $\text{SF}_6$ , see Figures 2 and 3. This is consistent with the increased interaction strength for  $\text{N}_2\text{O}$ - $\text{SF}_6$  as fewer solvent molecules are required to sufficiently perturb the system such as to illicit the change in the spectroscopy. Similarly, the slope of  $N(r)$  vs. concentration can also serve as a qualitative measure for the interaction strength. To stabilize a solvent shell of a certain size a smaller number (lower concentration) of solvent molecules is required if the solvent:solute interaction is sufficiently strong. These qualitative relationships are also reflected in the longer  $\tau_2$  values of the FFCFs for  $\text{N}_2\text{O}$  in  $\text{SF}_6$  compared with Xe as the solvent, see Figure 4.

## Conclusion

In conclusion, the present work establishes that the rotational structure of the asymmetric stretch band is quantitatively described for  $\text{N}_2\text{O}$  in xenon and is qualitatively captured in

SF<sub>6</sub> compared with experiment. Specifically, the change from P-/R-branches in the gas phase environment changes to a Q-branch-like structure, eventually assuming a Lorentzian-like lineshape once the solvent passes through the supercritical fluid to the liquid state. Transition between the gas- and SCF-like solvent is reflected in a steep increase in the longer correlation time  $\tau_2$  in the FFCF for both solvents. The radial distribution function becomes more structured as the density of the environment increases. The present work suggests that atomistic simulations together with machine learned and accurate electrostatic interactions yield a quantitative understanding of the spectroscopy and structural dynamics<sup>4</sup> from very low density to the liquid environment with the possibility to characterize transition to the SCF.

## Acknowledgment

This work was supported by the Swiss National Science Foundation grants 200021-117810, 200020-188724, the NCCR MUST, and the University of Basel (to MM) and by European Union’s Horizon 2020 research and innovation program under the Marie Skłodowska-Curie grant agreement No 801459 -FP-RESOMUS which is gratefully acknowledged. The support of the National Science Foundation grant CHE-2102427 (LDZ) and the Boston University Photonics Center is gratefully acknowledged. We thank James L. Skinner for valuable correspondence on Ref. 58.

## Data Availability

Raw data were generated at the University of Basel large scale facility. Derived data supporting the findings of this study are available from the corresponding author upon reasonable request. The data that allow to reproduce the findings of this study are openly available at [https://github.com/MMunibas/N20\\_SF6\\_Xe](https://github.com/MMunibas/N20_SF6_Xe).

## References

- (1) Stratt, R. M.; Maroncelli, M. Nonreactive dynamics in solution: The emerging molecular view of solvation dynamics and vibrational relaxation. *J. Phys. Chem.* **1996**, *100*, 12981–12996.
- (2) Turan, H. T.; Brickel, S.; Meuwly, M. Solvent Effects on the Menshutkin Reaction. *J. Phys. Chem. B* **2022**, *126*, 1951–1961.
- (3) Hamm, P.; Zanni, M. *Concepts and methods of 2D infrared spectroscopy*; Cambridge University Press, 2011.
- (4) Meuwly, M. Atomistic Simulations for Reactions and Vibrational Spectroscopy in the Era of Machine Learning - Quo Vadis? *J. Phys. Chem. B* **2022**, *126*, 2155–2167.
- (5) Guardiola, C.; Olmeda, P.; Pla, B.; Bares, P. In-cylinder pressure based model for exhaust temperature estimation in internal combustion engines. *Appl. Therm. Eng.* **2017**, *115*, 212–220.
- (6) Hessel, V.; Tran, N. N.; Asrami, M. R.; Tran, Q. D.; Long, N. V. D.; Escribà-Gelonch, M.; Tejada, J. O.; Linke, S.; Sundmacher, K. Sustainability of green solvents—review and perspective. *Green Chem.* **2022**,
- (7) Kajimoto, O. Solvation in Supercritical Fluids: Its Effects on Energy Transfer and Chemical Reactions. *Chem. Rev.* **1999**, *99*, 355–\*390.
- (8) Ž. Knez,; Markočič, E.; Leitgeb, M.; Primožič, M.; Knez Hrnčič, M.; Škerget, M. Industrial applications of supercritical fluids: A review. *Energy* **2014**, *77*, 235–243.
- (9) Töpfer, K.; Pasti, A.; Das, A.; Salehi, S. M.; Vazquez-Salazar, L. I.; Rohrbach, D.; Feurer, T.; Hamm, P.; Meuwly, M. Structure, Organization, and Heterogeneity of Water-Containing Deep Eutectic Solvents. *J. Am. Chem. Soc.* **2022**, *144*, 14170–14180.

- (10) Kuo, C.-H.; Vorobyev, D. Y.; Chen, J.; Hochstrasser, R. M. Correlation of the Vibrations of the Aqueous Azide Ion with the O-H Modes of Bound Water Molecules. *J. Phys. Chem. B* **2007**, *111*, 14028–14033.
- (11) Bian, H.; Wen, X.; Li, J.; Chen, H.; Han, S.; Sun, X.; Song, J.; Zhuang, W.; Zheng, J. Ion Clustering in Aqueous Solutions Probed with Vibrational Energy Transfer. *Proc. Natl. Acad. Sci.* **2011**, *108*, 4737–4742.
- (12) Bian, H.; Chen, H.; Li, J.; Wen, X.; Zheng, J. Nonresonant and Resonant Mode-Specific Intermolecular Vibrational Energy Transfers in Electrolyte Aqueous Solutions. *J. Phys. Chem. A* **2011**, *115*, 11657–11664.
- (13) Bian, H.; Li, J.; Zhang, Q.; Chen, H.; Zhuang, W.; Gao, Y. Q.; Zheng, J. Ion Segregation in Aqueous Solutions. *J. Phys. Chem. B* **2012**, *116*, 14426–14432.
- (14) Bian, H.; Chen, H.; Zhang, Q.; Li, J.; Wen, X.; Zhuang, W.; Zheng, J. Cation Effects on Rotational Dynamics of Anions and Water Molecules in Alkali ( $\text{Li}^+$ ,  $\text{Na}^+$ ,  $\text{K}^+$ ,  $\text{Cs}^+$ ) Thiocyanate ( $\text{SCN}^-$ ) Aqueous Solutions. *J. Phys. Chem. B* **2013**, *117*, 7972–7984.
- (15) Chen, H.; Bian, H.; Li, J.; Wen, X.; Zheng, J. Ultrafast Multiple-Mode Multiple-dimensional Vibrational Spectroscopy. *Int. Rev. Phys. Chem.* **2012**, *31*, 469–565.
- (16) Chen, H.; Wen, X.; Li, J.; Zheng, J. Molecular Distances Determined with Resonant Vibrational Energy Transfers. *J. Phys. Chem. A* **2014**, *118*, 2463–2469.
- (17) Chen, H.; Wen, X.; Guo, X.; Zheng, J. Intermolecular vibrational energy transfers in liquids and solids. *Phys. Chem. Chem. Phys.* **2014**, *16*, 13995–14014.
- (18) Fernández-Terán, R.; Hamm, P. A Closer Look Into the Distance Dependence of Vibrational Energy Transfer on Surfaces Using 2D ATR-IR Spectroscopy. *J. Chem. Phys.* **2020**, *153*, 154706.

- (19) Schirmer, R. E.; Noggle, J. H.; Davis, J. P.; Hart, P. A. Determination of Molecular Geometry by Quantitative Application of the Nuclear Overhauser Effect. *J. Am. Chem. Soc.* **1970**, *92*, 3266–3273.
- (20) Bell, R. A.; Saunders, J. K. Correlation of the Intramolecular Nuclear Overhauser Effect with Internuclear Distance. *Can. J. Chem.* **1970**, *48*, 1114–1122.
- (21) Stryer, L.; Haugland, R. P. Energy Transfer: A Spectroscopic Ruler. *Proc. Natl. Acad. Sci.* **1967**, *58*, 719–726.
- (22) Mandal, A.; Ng Pack, G.; Shah, P. P.; Erramilli, S.; Ziegler, L. D. Ultrafast Two-Dimensional Infrared Spectroscopy of a Quasifree Rotor: *J* Scrambling and Perfectly Anticorrelated Cross Peaks. *Phys. Rev. Lett.* **2018**, *120*, 103401.
- (23) Ng Pack, G.; Rotondaro, M. C.; Shah, P. P.; Mandal, A.; Erramilli, S.; Ziegler, L. D. Two-dimensional infrared spectroscopy from the gas to liquid phase: density dependent *J*-scrambling, vibrational relaxation, and the onset of liquid character. *Phys. Chem. Chem. Phys.* **2019**, *21*, 21249–21261.
- (24) Rotondaro, M. C.; Jain, A.; Erramilli, S.; Ziegler, L. D. Ultrafast 2DIR comparison of rotational energy transfer, isolated binary collision breakdown, and near critical fluctuations in Xe and SF<sub>6</sub> solutions. *J. Chem. Phys.* **2022**, *157*, 174305.
- (25) Devereux, M.; Raghunathan, S.; Fedorov, D. G.; Meuwly, M. A Novel, computationally efficient multipolar model employing distributed charges for molecular dynamics simulations. *J. Chem. Theo. Comp.* **2014**, *10*, 4229–4241.
- (26) Unke, O. T.; Devereux, M.; Meuwly, M. Minimal distributed charges: Multipolar quality at the cost of point charge electrostatics. *J. Chem. Phys.* **2017**, *147*, 161712.
- (27) Devereux, M.; Pezzella, M.; Raghunathan, S.; Meuwly, M. Polarizable Multipolar

- Molecular Dynamics Using Distributed Point Charges. *J. Chem. Theo. Comp.* **2020**, *16*, 7267–7280.
- (28) Unke, O. T.; Meuwly, M. Toolkit for the Construction of Reproducing Kernel-based Representations of Data: Application to Multidimensional Potential Energy Surfaces. *J. Chem. Inf. and Mod.* **2017**, *57*, 1923–1931.
- (29) Koner, D.; San Vicente Veliz, J. C.; Bemish, R. J.; Meuwly, M. Accurate reproducing kernel-based potential energy surfaces for the triplet ground states of N<sub>2</sub>O and dynamics for the N + NO ↔ O + N<sub>2</sub> and N<sub>2</sub> + O → 2N + O reactions. *Phys. Chem. Chem. Phys.* **2020**, *22*, 18488–18498.
- (30) Werner, H.-J.; Knowles, P. J.; Manby, F. R.; Black, J. A.; Doll, K.; Heßelmann, A.; Kats, D.; Köhn, A.; Korona, T.; Kreplin, D. A. et al. The Molpro quantum chemistry package. *J. Chem. Phys.* **2020**, *152*, 144107.
- (31) Dellis, D.; Samios, J. Molecular force field investigation for Sulfur Hexafluoride: A computer simulation study. *Fluid Phase Equilib.* **2010**, *291*, 81–89.
- (32) Aziz, R. A.; Slaman, M. On the Xe-Xe potential energy curve and related properties. *Mol. Phys.* **1986**, *57*, 825–840.
- (33) Stephenson, R. M.; Malanowski, S.; Ambrose, D. *Handbook of the thermodynamics of organic compounds; section on vapor-liquid critical constants of fluids*; Elsevier, 1987.
- (34) Haynes, W. *CRC Handbook of Chemistry and Physics*; CRC Handbook of Chemistry and Physics; CRC Press, 2014; p. 6-85.
- (35) Frisch, M. J.; Trucks, G. W.; Schlegel, H. B.; Scuseria, G. E.; Robb, M. A.; Cheeseman, J. R.; Scalmani, G.; Barone, V.; Petersson, G. A.; Nakatsuji, H. et al. Gaussian~16 Revision C.01. 2016; Gaussian Inc. Wallingford CT.

- (36) Olney, T. N.; Cann, N.; Cooper, G.; Brion, C. Absolute scale determination for photoabsorption spectra and the calculation of molecular properties using dipole sum-rules. *Chem. Phys.* **1997**, *223*, 59–98.
- (37) Gussoni, M.; Rui, M.; Zerbi, G. Electronic and relaxation contribution to linear molecular polarizability. An analysis of the experimental values. *J. Mol. Struct.* **1998**, *447*, 163–215.
- (38) Brooks, B. R.; Brooks III, C. L.; MacKerell Jr., A. D.; Nilsson, L.; Petrella, R. J.; Roux, B.; Won, Y.; Archontis, G.; Bartels, C.; Boresch, S. et al. CHARMM: The Biomolecular Simulation Program. *J. Comp. Chem.* **2009**, *30*, 1545–1614.
- (39) Ramírez, R.; López-Ciudad, T.; Kumar P, P.; Marx, D. Quantum corrections to classical time-correlation functions: Hydrogen bonding and anharmonic floppy modes. *J. Chem. Phys.* **2004**, *121*, 3973–3983.
- (40) Cho, M.; Fleming, G. R.; Saito, S.; Ohmine, I.; Stratt, R. M. Instantaneous normal mode analysis of liquid water. *J. Chem. Phys.* **1994**, *100*, 6672–6683.
- (41) Kalbfleisch, T. S.; Ziegler, L. D.; Keyes, T. An instantaneous normal mode analysis of solvation: Methyl iodide in high pressure gases. *J. Chem. Phys.* **1996**, *105*, 7034–7046.
- (42) Tennyson, J.; Kostin, M. A.; Barletta, P.; Harris, G. J.; Polyansky, O. L.; Ramanlal, J.; Zobov, N. F. DVR3D: a program suite for the calculation of rotation–vibration spectra of triatomic molecules. *Comput. Phys. Commun.* **2004**, *163*, 85–116.
- (43) Herzberg, G. *Infrared and Raman Spectra of Polyatomic Molecules*; D. Van Nostrand Company, Inc., New York, 1945.
- (44) Herzberg, G.; Herzberg, L. Rotation-Vibration Spectra of Diatomic and Simple Polyatomic Molecules with Long Absorbing Paths VI. The Spectrum of Nitrous Oxide ( $\text{N}_2\text{O}$ ) below  $1.2\mu$ . *J. Chem. Phys.* **1950**, *18*, 1551–1561.

- (45) Kagann, R. H. Infrared absorption intensities for N<sub>2</sub>O. *J. Mol. Spectrosc.* **1982**, *95*, 297–305.
- (46) Maddox, M. W.; Goodyear, G.; Tucker, S. C. Origins of Atom-Centered Local Density Enhancements in Compressible Supercritical Fluids. *J. Phys. Chem. B* **2000**, *104*, 6248–6257.
- (47) Maddox, M. W.; Goodyear, G.; Tucker, S. C. Effect of Critical Slowing Down on Local-Density Dynamics. *J. Phys. Chem. B* **2000**, *104*, 6266–6270.
- (48) Linstorm, P. NIST chemistry webbook, NIST standard reference database number 69. *J. Phys. Chem. Ref. Data, Monograph* **1998**, *9*, 1–1951.
- (49) Salehi, S. M.; Koner, D.; Meuwly, M. Vibrational Spectroscopy of N<sub>3</sub><sup>-</sup> in the Gas and Condensed Phase. *J. Phys. Chem. B* **2019**, *123*, 3282–3290.
- (50) Koziński, M.; Garrett-Roe, S.; Hamm, P. Vibrational spectral diffusion of CN<sup>-</sup> in water. *Chem. Phys.* **2007**, *341*, 5–10.
- (51) Lee, M. W.; Carr, J. K.; Göllner, M.; Hamm, P.; Meuwly, M. 2D IR spectra of cyanide in water investigated by molecular dynamics simulations. *J. Chem. Phys.* **2013**, *139*, 054506.
- (52) Maekawa, H.; Ohta, K.; Tominaga, K. Vibrational dynamics in liquids studied by non-linear infrared spectroscopy. *Res Chem. Interm.* **2005**, *31*, 703–716.
- (53) Levesque, D.; Weis, J.-J.; Oxtoby, D. W. A molecular dynamics simulation of rotational and vibrational relaxation in liquid HCl. *J. Chem. Phys.* **1983**, *79*, 917–925.
- (54) Chesnoy, J.; Gale, G. Vibrational energy relaxation in liquids. *Ann. Phys.* **1984**, *9*, 893–949.

- (55) Adelman, S.; Muralidhar, R.; Stote, R. Time correlation function approach to vibrational energy relaxation in liquids: Revised results for monatomic solvents and a comparison with the isolated binary collision model. *J. Chem. Phys.* **1991**, *95*, 2738–2751.
- (56) Berens, P. H.; Wilson, K. R. Molecular dynamics and spectra. I. Diatomic rotation and vibration. *J. Chem. Phys.* **1981**, *74*, 4872–4882.
- (57) Padilla, A.; Pérez, J.; Herrebout, W.; Van der Veken, B.; Bulanin, M. A simulation study of the vibration–rotational spectra of HCl diluted in Ar: Rotational dynamics and the origin of the Q-branch. *J. Mol. Struct.* **2010**, *976*, 42–48.
- (58) Hestand, N. J.; Strong, S. E.; Shi, L.; Skinner, J. L. Mid-IR spectroscopy of supercritical water: From dilute gas to dense fluid. *J. Chem. Phys.* **2019**, *150*, 054505.
- (59) Chabbi, H.; Dahoo, P. R.; Gauthier-Roy, B.; Vasserot, A.; Abouaf-Marguin, L. Infrared Stimulated Emission of N<sub>2</sub>O Trapped in Argon Matrices: Comparison with O<sub>3</sub> and CO<sub>2</sub>. *J. Phys. Chem. A* **2000**, *104*, 1670–1673.
- (60) Li, X.; Liu, Z.; Duan, C. Rovibrational spectra of nonpolar (N<sub>2</sub>O)<sub>2</sub> and Ar–N<sub>2</sub>O complexes in the 2ν<sub>2</sub> overtone region of N<sub>2</sub>O. *J. Mol. Spectrosc.* **2021**, *377*, 111424.
- (61) Rost, J. M.; Griffin, J. C.; Friedrich, B.; Herschbach, D. R. Pendular states and spectra of oriented linear molecules. *Phys. Rev. Lett.* **1992**, *68*, 1299–1302.
- (62) Block, P. A.; Bohac, E. J.; Miller, R. E. Spectroscopy of pendular states: The use of molecular complexes in achieving orientation. *Phys. Rev. Lett.* **1992**, *68*, 1303–1306.
- (63) Ashbaugh, M. S.; Chicone, C. C.; Cushman, R. H. The twisting tennis racket. *J. Dyn. Differ. Equation* **1991**, *3*, 67–85.
- (64) Tidwell, E. D.; Plyler, E. K.; Benedict, W. S. Vibration-Rotation Bands of N<sub>2</sub>O\*. *J. Opt. Soc. Am.* **1960**, *50*, 1243–1263.

# Supporting Information: Molecular-Level Understanding of the Ro-vibrational Spectra of N<sub>2</sub>O in Gaseous, Supercritical and Liquid SF<sub>6</sub> and Xe

Kai Töpfer,<sup>†</sup> Debasish Koner,<sup>†,¶</sup> Shyamsunder Erramilli,<sup>‡</sup> Lawrence D. Ziegler,<sup>‡</sup>  
and Markus Meuwly<sup>\*,†,§</sup>

<sup>†</sup>*Department of Chemistry, University of Basel, Klingelbergstrasse 80, CH-4056 Basel,  
Switzerland*

<sup>‡</sup>*Department of Chemistry and the Photonics Center, Boston University, 8 St Mary's St,  
MA 02215, Boston*

<sup>¶</sup>*Department of Chemistry, Indian Institute of Technology Hyderabad, Sangareddy,  
Telangana 502285, India*

<sup>§</sup>*Department of Chemistry, Brown University, Providence, RI 02912, USA*

E-mail: m.meuwly@unibas.ch

# System Setup

**Table S1: System setup of N<sub>2</sub>O concentration  $c(\text{N}_2\text{O})$ , molar volumes  $V_m$  and critical density ratio  $\rho^*$  of one N<sub>2</sub>O in 343 SF<sub>6</sub> molecules and one N<sub>2</sub>O in 600 Xe atoms.**

N <sub>2</sub> O/SF <sub>6</sub>			N <sub>2</sub> O/Xe		
$c(\text{N}_2\text{O})$ (mol/l)	$V_m(\text{SF}_6)$ (cm <sup>3</sup> /mol)	$\rho^*$	$c(\text{N}_2\text{O})$ (mol/l)	$V_m(\text{Xe})$ (cm <sup>3</sup> /mol)	$\rho^*$
0.20	4934	0.04	0.34	2984	0.04
0.51	1974	0.10	0.84	1194	0.10
0.81	1234	0.16	1.26	796	0.15
1.52	658	0.30	3.10	323	0.37
3.39	295	0.67	4.11	244	0.49
4.36	229	0.86	5.19	193	0.62
5.02	199	0.99	5.53	181	0.66
5.93	169	1.17	6.28	159	0.75
6.89	145	1.36	7.29	137	0.87
7.65	131	1.51	7.79	128	0.93
			11.14	90	1.33
			12.99	77	1.55

**Table S2: Bonded and non-bonded parameters. Larger sets of parameters are made available on a github as full parameter files.**

Residues	Parameters	
<b>N<sub>2</sub>O</b>		
Intramolecular Potential RKHS <sup>1</sup>	<a href="https://github.com/MMunibas/N2O_SF6_Xe/">https://github.com/MMunibas/N2O_SF6_Xe/</a> in, e.g., N2O_Xe/source/pes1_rRz.csv or N2O_SF6/source/pes1_rRz.csv	
Electrostatic Potential polarizable MDCM <sup>2</sup>	<a href="https://github.com/MMunibas/N2O_SF6_Xe/">https://github.com/MMunibas/N2O_SF6_Xe/</a> in, e.g., N2O_Xe/source/n2o_xe.dcm or N2O_SF6/source/n2o_sf6.dcm	
Non-bonded in SF <sub>6</sub>	$\epsilon_i$ (kcal/mol)	$R_{\min,i}/2$ (Å)
N1	0.2592	1.716
N2	0.1542	1.618
O	0.2089	1.555
Non-bonded in Xe	$\epsilon_i$ (kcal/mol)	$R_{\min,i}/2$ (Å)
N1	0.3775	1.637
N2	0.0002	2.565
O	0.3684	1.497
<b>SF<sub>6</sub></b>	Samios and coworker <sup>3</sup>	
Bonds	$k_b$ (kcal/mol/Å <sup>2</sup> )	$r_{\min}$ (Å)
S-F	165.746	1.565
Angles	$k_{\Theta}$ (kcal/mol/rad <sup>2</sup> )	$\Theta_{\min}$ (°)
F-S-F	73.461	90.0
Electrostatic Potential polarizable MDCM <sup>2</sup> *	<a href="https://github.com/MMunibas/N2O_SF6_Xe/">https://github.com/MMunibas/N2O_SF6_Xe/</a> in, e.g., N2O_Xe/source/n2o_xe.dcm or N2O_SF6/source/n2o_sf6.dcm	
Non-bonded	$\epsilon_i$ (kcal/mol)	$R_{\min,i}/2$ (Å)
S	0.3257	1.822
F	0.0541	1.659
<b>Xe</b>	Aziz and coworker <sup>4</sup>	
Electrostatic Potential polarizable MDCM <sup>2</sup> **	$q$ (e)	$\alpha$ (1/Å <sup>3</sup> )
	0.0	2.964
Non-bonded Xe	$\epsilon_i$ (kcal/mol)	$R_{\min,i}/2$ (Å)
	0.5610	2.181

\* Contributing only to N<sub>2</sub>O-SF<sub>6</sub> interaction

\*\* Contributing effectively only to N<sub>2</sub>O-Xe interaction

# Local Solvent Reorganization Lifetime

The local solvent reorganization lifetime can be used as a proxy to determine the critical concentration (density) at which transition so a SCF occurs.<sup>5,6</sup>

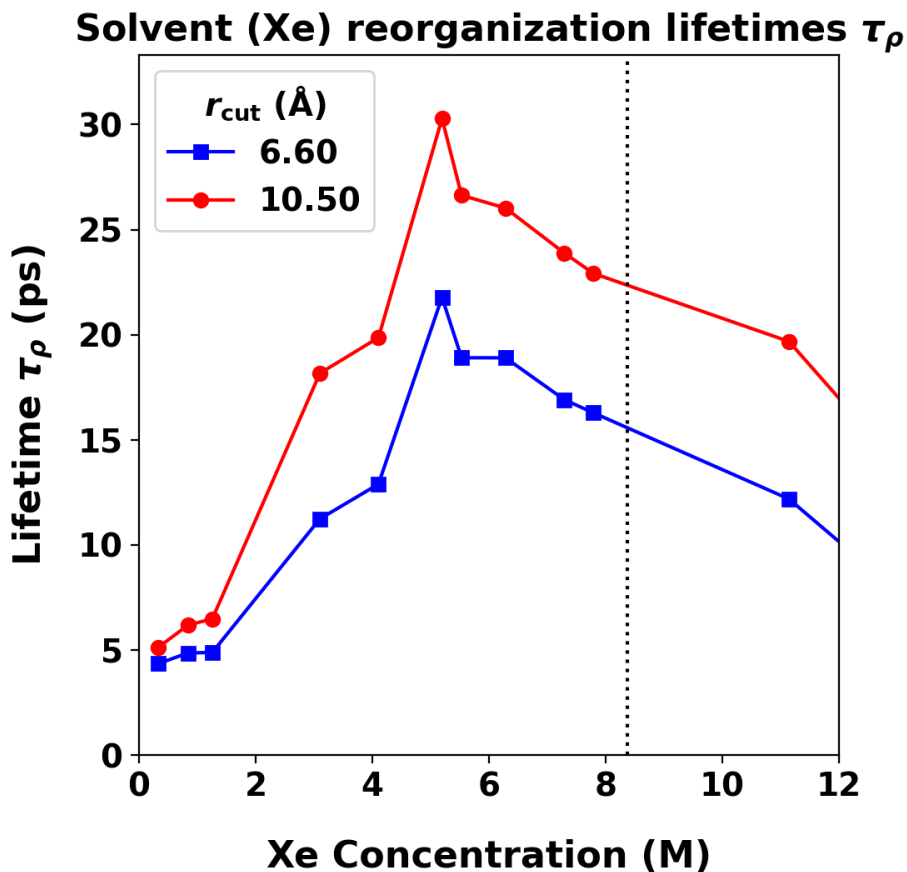


Figure S1: Local solvent reorganization lifetime  $\tau_\rho$  from MD simulations of pure Xenon (600 atoms) at  $T = 291.2$  K. The lifetime is computed following the work by Tucker *et al.*<sup>5,6</sup> for two cutoff radii  $r_{\text{cut}} = 6.6, 10.5$  Å for the first and second solvation shells, respectively. These radii correspond to the local minima of the Xe–Xe radial distribution function, see Figure S4A. The peak in  $\tau_\rho$  as a function of concentration at  $c(\text{Xe}) = 5.19$  M compares with an experimentally determined critical concentration of  $c(\text{Xe}) = 8.45$  M (dotted vertical line).<sup>7</sup> This difference arises due to the fact that the parametrization of the Xe–Xe interaction potential was carried out exclusively based on reference data from the gas phase.<sup>4</sup>

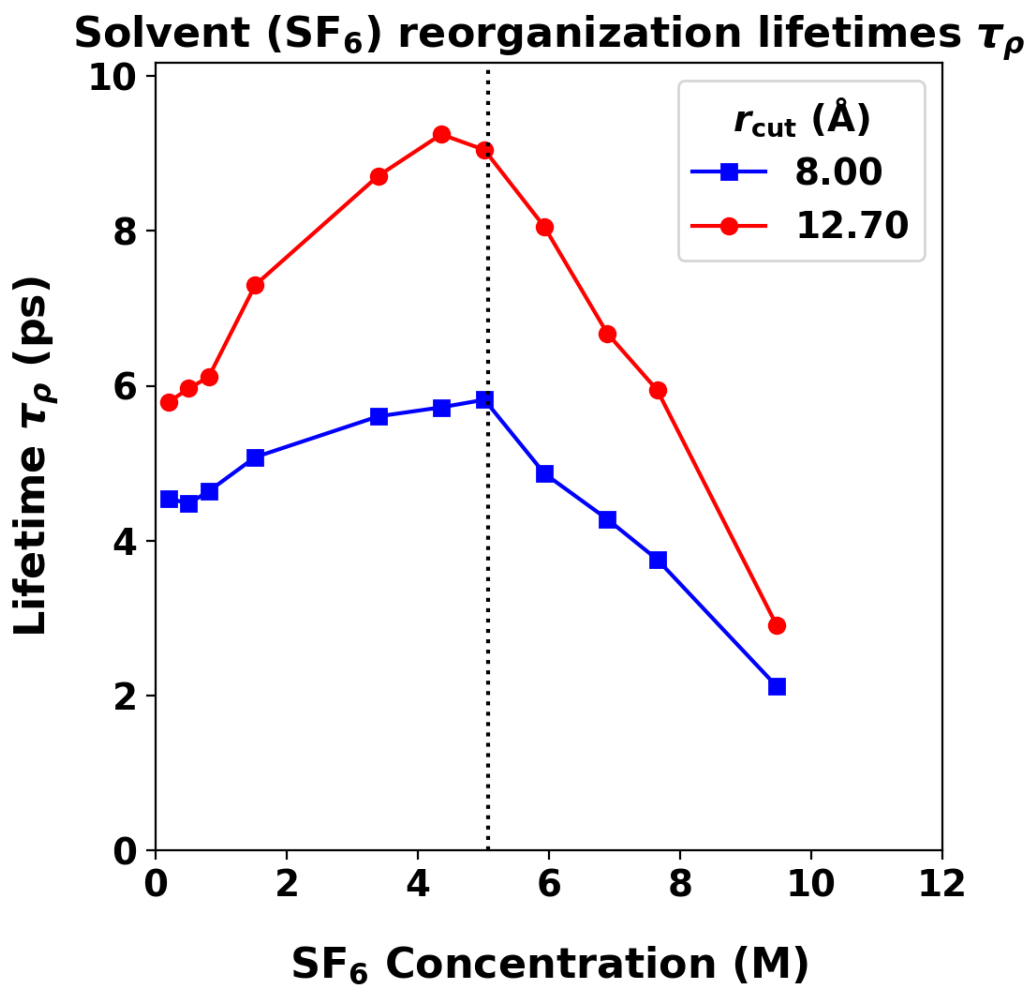


Figure S2: Local solvent reorganization lifetime  $\tau_\rho$  from MD simulations of pure SF<sub>6</sub> (343 molecules) at  $T = 321.9$  K. The lifetime is computed following the work by Tucker *et al.*<sup>5,6</sup> for two cutoff radii  $r_{\text{cut}} = 8.0, 12.7$  Å of the first and second solvation shells, respectively. These radii correspond to the local minima of the SF<sub>6</sub>-SF<sub>6</sub> radial distribution function, see Figure S4B. The peak in  $\tau_\rho$  for  $r_{\text{cut}} = 8.0$  at  $c(\text{SF}_6) = 5.02$  M agrees with the experimentally observed<sup>7</sup> critical concentration for SF<sub>6</sub> at  $c(\text{SF}_6) = 5.06$  M at  $T = 318.76$  K.

# Radial Distribution Functions

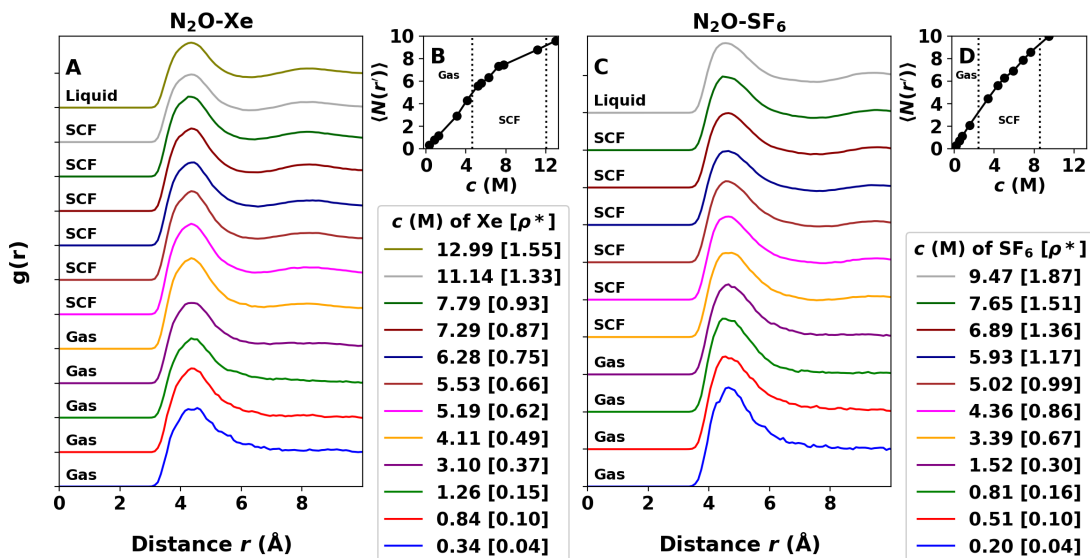


Figure S3: Radial distribution function  $g(r)$  between  $N_2O$  solutes center of mass and (A) the Xe atom and (C) the sulfur atom of  $SF_6$  at different solvent concentrations. Panels B and D show the coordination number of the Xe and  $SF_6$  solvent compounds within the first solvation shell around  $N_2O$  of about (B)  $r' = 6.5 \text{ \AA}$  and (D)  $r' = 7.5 \text{ \AA}$ . The vertical dotted lines mark the approximate concentrations of the solvent phase transition.

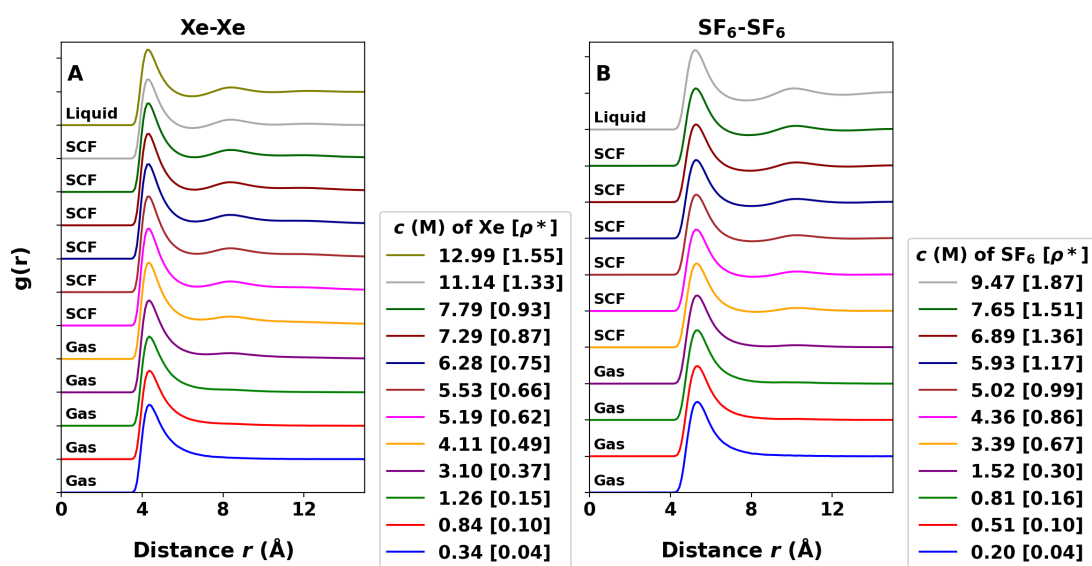


Figure S4: Solvent-solvent radial distribution functions  $g_{SS}(r)$  for (A) Xe and (B) SF<sub>6</sub> with the sulfur atom as the reference at different solvent concentrations.

# Infrared Spectra

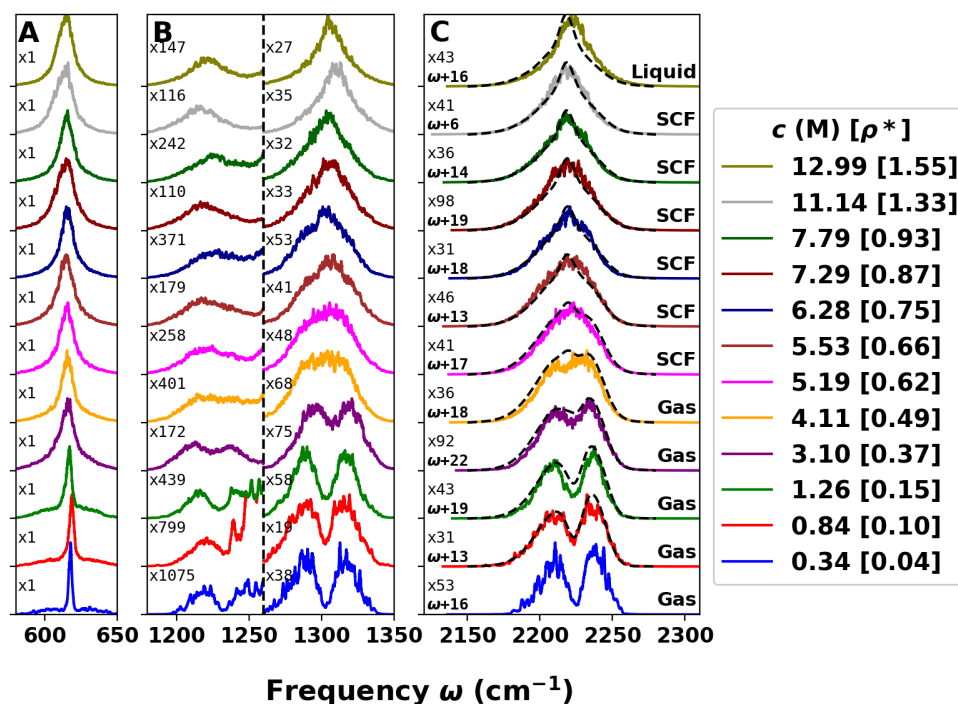


Figure S5: IR spectra of N<sub>2</sub>O in xenon at different solvent concentrations frequency ranges of (A) 580-650 cm<sup>-1</sup>, (B) 1180-1350 cm<sup>-1</sup> and (C) 2120-2310 cm<sup>-1</sup> at 291.2 K. The amplitudes are scaled by the factor indicated at the center left for each range and density. The amplitude of the line shape in Panel B are separately scaled for hot band and symmetric stretch on the left and right of the black dashed line, respectively. In the right column, the line shape frequency bands are shifted in frequency  $\omega$  to maximize the overlap with the experimental IR signal (dashed black lines, at 291 K for gas, SCF, and at 287 K for liquid xenon) at the corresponding density for the N<sub>2</sub>O asymmetric stretch vibration. The frequency shift is also given in the bottom left corner, and an average shift is applied for densities without experimental reference spectra.

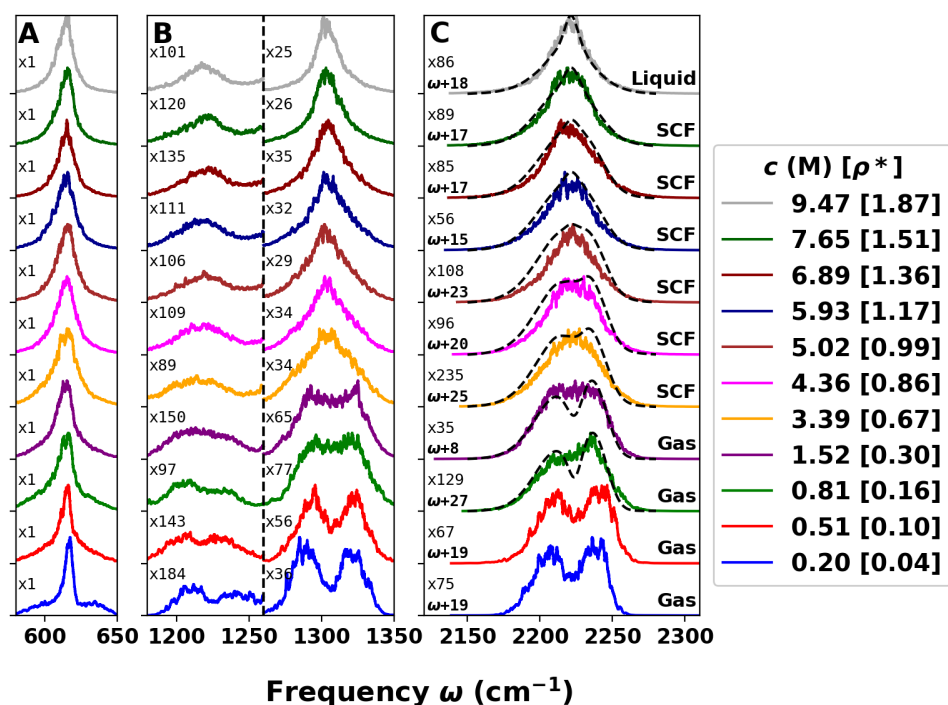


Figure S6: IR spectra of  $\text{N}_2\text{O}$  in  $\text{SF}_6$  at different solvent concentrations frequency ranges of (A)  $580\text{-}650\text{ cm}^{-1}$ , (B)  $1180\text{-}1350\text{ cm}^{-1}$  and (C)  $2120\text{-}2310\text{ cm}^{-1}$  at  $291.2\text{ K}$ . The amplitudes are scaled by the factor indicated at the center left for each range and density. The amplitude of the line shape in Panel B are separately scaled for hot band and symmetric stretch on the left and right of the black dashed line, respectively. In the right column, the line shape frequency bands are shifted in frequency  $\omega$  to maximize the overlap with the experimental IR signal (dashed black lines, at  $322\text{ K}$  for gas, SCF, and at  $293\text{ K}$  for liquid  $\text{SF}_6$ ) at the corresponding density for the  $\text{N}_2\text{O}$  asymmetric stretch vibration. The frequency shift is also given in the bottom left corner, and an average shift is applied for densities without experimental reference spectra.

# Frequency-Frequency Correlation Function

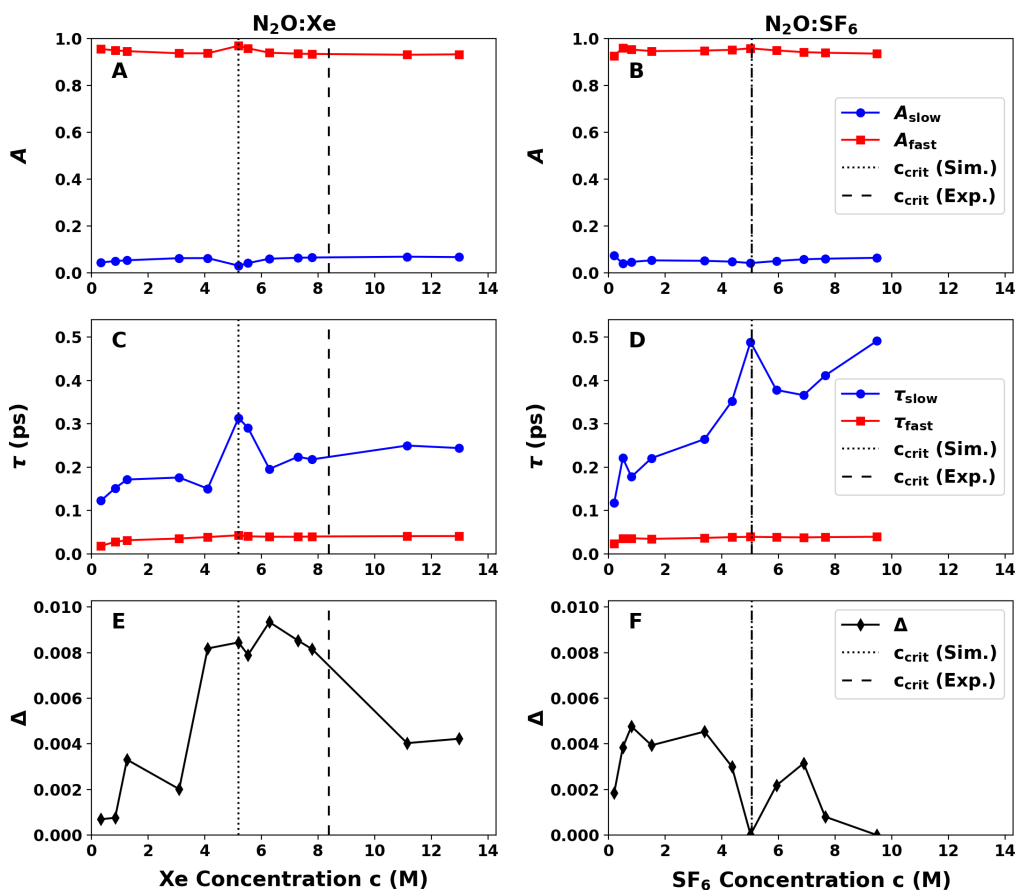


Figure S7: Amplitudes ( $a_1$  and  $a_2$ ), decay times ( $\tau_1$  and  $\tau_2$ ), and asymptotic values ( $\Delta$ ) for the bi-exponential fits for  $\text{N}_2\text{O}$  in  $\text{Xe}$  (A, C, E) and  $\text{SF}_6$  (B, D, F) depending on solvent concentration. The experimental<sup>7</sup> critical concentration  $c_{\text{crit}}$  and from simulations at  $T_c$  of xenon and  $\text{SF}_6$ , are marked by the vertical dashed and dotted line, respectively. It should be noted that the Xe–Xe interactions<sup>4</sup> were not optimized to reproduce the experimentally known  $T_c$  for pure Xe whereas the model for  $\text{SF}_6$  does.

# Instantaneous Normal Modes

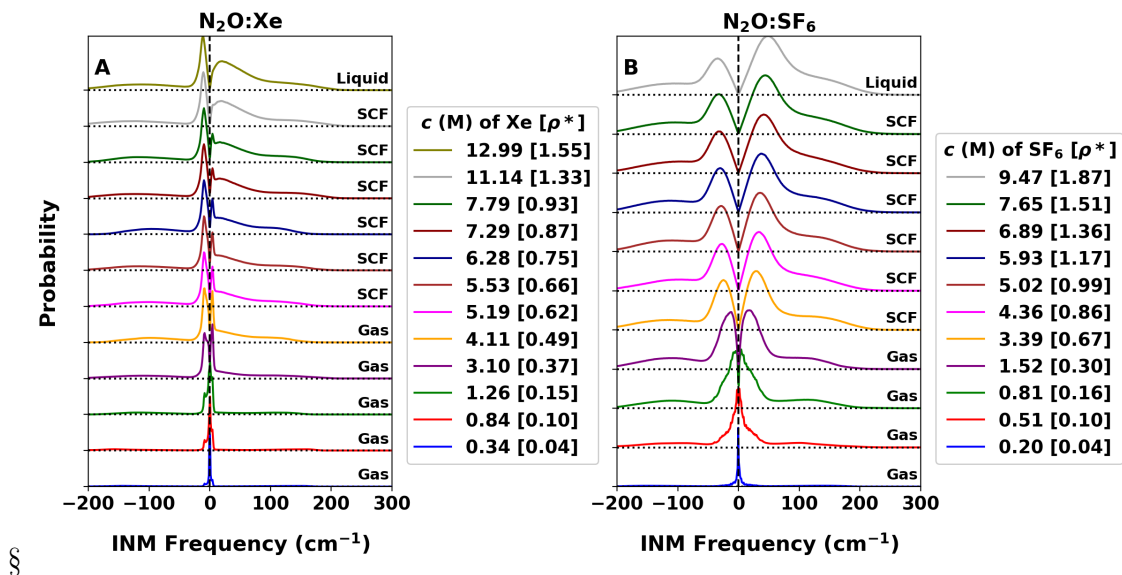


Figure S8: Histogram of low-frequencies instantaneous normal modes frequencies of  $\text{N}_2\text{O}$  without prior geometry optimization in (A) xenon and (B)  $\text{SF}_6$  at different solvent concentrations. The vertical dashed line marks the zero position in the frequency range and the horizontal dotted line shows the zero probability for each solvent density to guide the eye.

## References

- (1) Koner, D.; San Vicente Veliz, J. C.; Bemish, R. J.; Meuwly, M. Accurate reproducing kernel-based potential energy surfaces for the triplet ground states of N<sub>2</sub>O and dynamics for the N + NO  $\leftrightarrow$  O + N<sub>2</sub> and N<sub>2</sub> + O  $\rightarrow$  2N + O reactions. *Phys. Chem. Chem. Phys.* **2020**, *22*, 18488–18498.
- (2) Devereux, M.; Pezzella, M.; Raghunathan, S.; Meuwly, M. Polarizable Multipolar Molecular Dynamics Using Distributed Point Charges. *J. Chem. Theo. Comp.* **2020**, *16*, 7267–7280.
- (3) Dellis, D.; Samios, J. Molecular force field investigation for Sulfur Hexafluoride: A computer simulation study. *Fluid Phase Equilib.* **2010**, *291*, 81–89.
- (4) Aziz, R. A.; Slaman, M. On the Xe-Xe potential energy curve and related properties. *Mol. Phys.* **1986**, *57*, 825–840.
- (5) Maddox, M. W.; Goodyear, G.; Tucker, S. C. Origins of Atom-Centered Local Density Enhancements in Compressible Supercritical Fluids. *J. Phys. Chem. B* **2000**, *104*, 6248–6257.
- (6) Maddox, M. W.; Goodyear, G.; Tucker, S. C. Effect of Critical Slowing Down on Local-Density Dynamics. *J. Phys. Chem. B* **2000**, *104*, 6266–6270.
- (7) Haynes, W. *CRC Handbook of Chemistry and Physics*; CRC Handbook of Chemistry and Physics; CRC Press, 2014; p. 6-85.